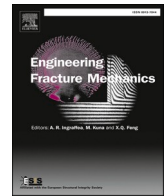




ELSEVIER

Contents lists available at ScienceDirect

Engineering Fracture Mechanics

journal homepage: www.elsevier.com/locate/engfracmech

A 2D continuous-discontinuous heat transport model considering thermal cracking for the combined finite-discrete element method (FDEM) using node binding scheme

Weibing Cai^{a,c}, Ke Gao^{a,b,*}, Shugang Ai^a, Shuai Zhang^a, Yu Feng^{d,e,*}

^a Department of Earth and Space Sciences, Southern University of Science and Technology, Shenzhen 518055 Guangdong, China

^b SUSTech Energy Institute for Carbon Neutrality, Southern University of Science and Technology, Shenzhen 518055 Guangdong, China

^c Department of Civil and Systems Engineering, Johns Hopkins University, Baltimore 21218 MD, USA

^d School of Civil Engineering, Sun Yat-sen University, Zhuhai 519082 Guangdong, China

^e State Key Laboratory for Tunnel Engineering, Sun Yat-sen University, Guangzhou 510275, China

ARTICLE INFO

Keywords:

Combined finite-discrete element method (FDEM)

Node binding scheme

Heat conduction

Heat transfer

Thermal cracking

ABSTRACT

Within the framework of the combined finite-discrete element method (FDEM) employing cohesive elements, we propose a novel thermo-mechanical coupling model to simulate heat transport in fractured rock masses (i.e., heat conduction, heat transfer and heat exchange) and capture the initiation and propagation of thermal cracking. Instead of using a fictitious heat exchange coefficient for cohesive elements as those in previous work, in this model, we adopt a node binding scheme to ensure the continuity of heat conduction in the intact/continuous rock matrix domain prior to fracturing. The computational efficiency of heat conduction using the proposed approach is significantly improved ~ 110 times (about 2560 triangle elements contained in a model), and the extra numerical parameter (i.e., the heat exchange coefficient of cohesive element) commonly used in the conventional FDEM is not required. To accommodate the finite strain theory implemented in FDEM for large deformations and rotations, we also employ the multiplicative decomposition of deformation gradient to calculate the thermal stress. We conduct a suite of numerical benchmarks to verify the effectiveness and robustness of the thermo-mechanical coupling model in terms of heat conduction, thermal cracking and heat transfer. As an application, a typical example is performed to uncover the underlying mechanism of thermal cracking induced by different temperatures and investigate the micro-fracturing of brittle crystalline rocks. The coupled thermo-mechanical coupling model may help enhance the applicability and accuracy of FDEM for deep energy exploitation.

1. Introduction

In the exploitation of deep geothermal energy, thermal cracks are often induced by the different thermal expansion coefficients of materials or thermal shock, which has been regarded as one origin of enhanced rock permeability by forming complex fracture networks at high temperatures [1]. As the target formation for nuclear waste storage, the rock masses are exposed to long-term elevated

* Corresponding authors at: Department of Earth and Space Sciences, Southern University of Science and Technology, Shenzhen 518055, Guangdong, China (K. Gao).

E-mail addresses: gaok@sustech.edu.cn (K. Gao), fengy253@mail.sysu.edu.cn (Y. Feng).

<https://doi.org/10.1016/j.engfracmech.2025.111365>

Received 3 February 2025; Received in revised form 24 May 2025; Accepted 25 June 2025

Available online 26 June 2025

0013-7944/© 2025 Elsevier Ltd. All rights are reserved, including those for text and data mining, AI training, and similar technologies.

Nomenclature

E	Young's modulus
ρ	Bulk density
ν	Poisson's ratio
T	Solid temperature
\mathbf{q}	Heat flow rate
Q_{ex}	Heat source per unit area/volume
A	Area of the triangle element
m_k, M_s	Mass of slave/master node
L_{min}	Minimum finite element size
Q_{con}	Contact heat transfer flux
T_s, T_f	Boundary temperature of solid and fluid
\mathbf{F}	Deformation gradient tensor
\mathbf{F}_t	Thermal component of \mathbf{F}
\mathbf{F}_e	Elastic component of \mathbf{F}
ΔT	Temperature change of a finite element
σ_{ij}	Cauchy stress tensor
λ, ξ	Lame constants
B_{ij}	Left Cauchy-Green deformation tensor
D_{ij}	Rate of deformation tensor
δ_{ij}	Kronecker delta
κ	Thermal diffusion coefficient
\mathbf{M}_{ij}	AE moment tensor
m_i^*	Deviatoric eigenvalues
R	The isotropic/deviatoric ratio
η	Viscous damping coefficient
k	Thermal conductivity coefficient
C_p	Heat capacity
α	Thermal expansion coefficient
h_c	Contact conductance coefficient
Δt_s	Solid time step
Δt_h	Thermal time step

temperatures induced by heat release during the decay process of nuclear waste [2], thereby producing thermal crack initiation and radionuclide migration contamination. Such highly complex processes involve heat conduction in rock matrix, thermally induced cracking, and heat contact between discrete bodies or fracture surfaces. Therefore, establishing a robust numerical model to adequately capture the thermo-mechanical responses associated with the progressive failure of rock masses is crucial to enhance energy production and ensure the safety of nuclear waste storage.

Generally, the thermo-mechanical coupling models can be classified into two categories, i.e., continuum-based and discontinuum-based approaches. Continuum-based approaches, such as the finite element method (FEM) [3], boundary element method (BEM) [4] and finite difference method (FDM) [5], can effectively simulate heat conduction in continuous medium and regard the plastic or damage elements as thermal cracks. However, those methods may fail to explicitly capture the propagation and coalescence of multiple cracks induced by thermal shock. As improvements, advanced numerical methodologies have been proposed, such as the extended finite element method (XFEM) [6], phase-field method [7], and peridynamic (PD) [8]. These approaches can simultaneously consider both heat conduction and thermal cracking; however, the heat transfer between fracture surfaces and the effect of fracture aperture on temperature evolution cannot be straightforwardly and explicitly captured.

For the discontinuum-based approach, commonly referred to as the discrete element method (DEM), the rock matrix is viewed as an assembly of particles or blocks bonded by spring with normal and tangential stiffness [9]. The commercial PFC (Particle Flow Code) software developed based on particle DEM has broad applications in brittle rock-related simulations. However, the heat conduction in DEM is independent of the mechanical response because the thermal expansion is approximately achieved by changing the radius of circle/sphere, thereby yielding inaccurate evaluations of thermal stress [10,11]. Furthermore, the temperature of particles across a fracture is considered continuous, which ignores the effect of cracks on heat conduction. Similar criticism has also been found for other commercial and research codes such as UDEC (Universal Distinct Element Code) [12] and DDA (Discontinuous Deformation Analysis) [13].

To simulate the fracturing behavior of brittle materials evolving from continuum to discontinuum, Munjiza [14] proposed the combined finite–discrete element method (FDEM), which merges the continuum analysis using FEM and the discontinuous simulations using DEM. In FDEM, the modeling domain is first discretized into a series of individual finite elements, and then zero-thickness cohesive elements are initially inserted into the common boundaries between adjacent finite elements before the onset of

simulation [15]. Within the framework of FDEM, Yan and Zheng [16] first proposed a 2D coupled thermo-mechanical model to simulate the thermal cracking of rock masses. This model introduces a large fictitious heat exchange coefficient for cohesive elements to enforce the continuity of heat conduction in the intact/continuous rock matrix domain prior to fracturing. Theoretically, their heat conduction results between adjacent finite elements can match the analytical solution in the continuous medium only if an infinite heat exchange coefficient is used. However, in practice, a large heat exchange coefficient for cohesive elements can result in smaller time steps and thus significantly increase the computational cost. Recently, Sun et al. [17] proposed a 2D coupled thermo-mechanical model that considers the anisotropy of the thermal expansion coefficient to investigate the heat conduction and thermal cracking process in anisotropic shale formations. Additionally, a contact heat transfer model is developed to capture the heat transfer between discrete bodies [18,19]. However, the heat exchange coefficient of cohesive elements has also been adopted in these recently developed thermo-mechanical models. Although efforts have been made to circumvent this deficiency by dynamically updating the node-sharing connections of the neighboring elements [20,21], unfortunately, the implementation details are unclear in the literature.

Here, based on our 2D in-house FDEM code – Pamuco, we draw a strategy from the node binding scheme proposed in our previous work [22] and introduce a continuous-discontinuous heat conduction model to ensure temperature continuity between adjacent finite elements in the intact/continuous rock matrix domain prior to fracturing. This method can avoid complex selection and calibration of the heat exchange coefficient for cohesive elements and also consider the effect of the newly generated fractures on heat conduction. Importantly, this approach can increase the computational efficiency of heat conduction simulation compared to the original thermo-mechanical coupling model [18,23,24] and effectively captures the heat transfer between discrete bodies or fracture surfaces. To consider the large deformation and rotations induced by temperatures, the multiplicative decomposition of the deformation gradient is also adopted to calculate thermal stresses [25,26].

The rest of the paper is organized as follows. In Section 2, we propose the thermo-mechanical coupling model in the current framework of FDEM. In Section 3, a series of benchmark cases are conducted to verify the accuracy and robustness of the proposed model. We also demonstrate the advantage of the proposed approach in terms of computational efficiency by performing a heat conduction test in Section 3.4. Following this, in Section 4, an application case is conducted to demonstrate the potential of the proposed approach in investigating the micro-thermal cracking of crystalline rocks. Conclusions are drawn in Section 5.

2. Thermo-mechanical model

In this section, the new thermo-mechanical coupling model is proposed to achieve the smooth transition of heat conduction from continuum to discontinuum using the node binding scheme. We also introduce a thermal contact model to capture the heat transfer between discrete bodies or adjacent fracture surfaces. Following this, we employ the multiplicative decomposition of the deformation gradient to calculate thermal stresses, which aligns with the finite strain framework of FDEM.

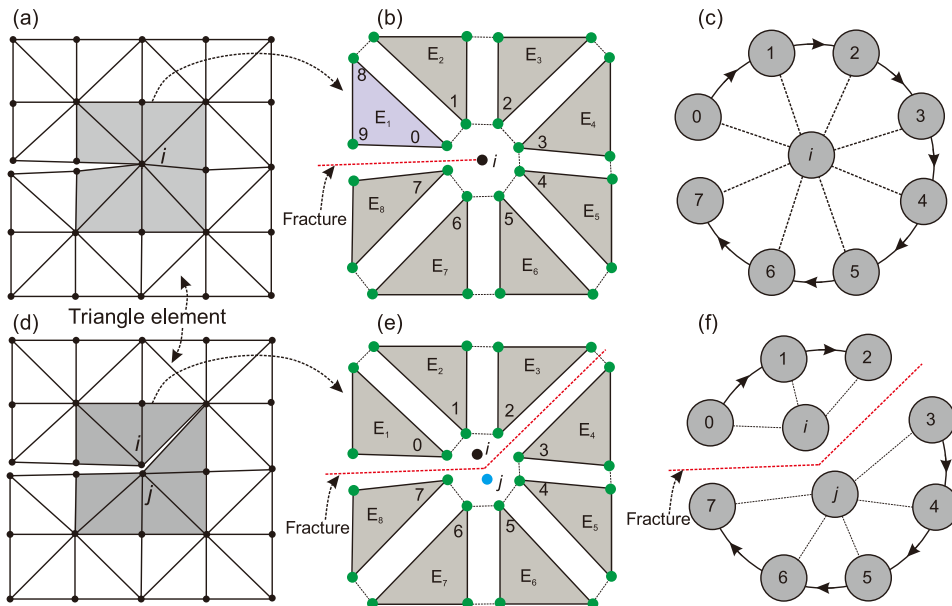


Fig. 1. Mesh discretization and update of the master–slave node mapping list and slave node group linked lists. Nodes 0 to 7 are slave nodes bound together as a group identified by master Nodes i and j . The triangle finite elements are marked as $E_1, E_2, E_3, E_4, E_5, E_6, E_7$ and E_8 in clockwise order, and the fracture is marked by the red dashed line. (For interpretation of the references to colour in this figure legend, the reader is referred to the web version of this article.)

2.1. Continuum heat conduction model

To ensure the continuum behavior of heat conduction considering crack propagation in brittle materials and further enhance the computational efficiency, the node binding scheme proposed in our previous work [22] is employed here to avoid using the fictitious parameter of heat exchange coefficient between adjacent finite elements in intact/continuous rock deformation domain. Prior to simulation, as shown in Fig. 1a-b, the solid domains of a rock model are discretized into triangle elements and then separated into independent elements without sharing nodes. The mapping information from the original nodes before mesh discretization (denoted as master nodes, e.g., Node i in Fig. 1a) to the corresponding new nodes after mesh discretization (denoted as slave nodes, e.g., Nodes 0 to 7 in Fig. 1b) is reserved in a master–slave manner. Each master node corresponds to one or several slave nodes, forming a master–slave group. We saved this mapping information between the master and slave nodes in a list such as $0 \rightarrow i, 1 \rightarrow i, \dots, 7 \rightarrow i$ (Fig. 1c). If a master node is located at the fracture tips, its slave nodes will be stored in an open linked list according to their relative positions, e.g., $0 \rightarrow 1 \rightarrow 2 \rightarrow 3 \rightarrow 4 \rightarrow 5 \rightarrow 6 \rightarrow 7$ (e.g., master node i in Fig. 1c). It is worth noting that the master nodes from the original mesh are merely used as identifiers for each slave node group.

To avoid heat exchange between adjacent finite elements by introducing additional numerical parameters (i.e., the heat exchange coefficient of cohesive element) during the intact/continuous deformation domain, we bind the slave nodes belonging to the same master node in each group. The heat flux and nodal masses of slave nodes in each group are all accumulated to their master node. At the end of each iteration, the slave nodes in the same group will share identical information (e.g., temperature) with their master node. Therefore, we only need to calculate the heat conduction in the triangle elements using Fourier's law, which can effectively reduce the computational cost (as will be discussed in Section 3.4). The governing equation of solid heat conduction based on energy conservation is given by [27]

$$\rho C_p \frac{\partial T}{\partial t} + \nabla \cdot \mathbf{q} = Q_{\text{ext}} \quad (1)$$

where ∇ denotes the gradient operator, ρ is the bulk density, C_p is the heat capacity, \mathbf{q} is the heat flow rate of the solid matrix, and Q_{ext} is the heat source per unit area/volume.

For each independent triangle element (e.g., $\Delta 089$ in Fig. 1b), the heat flux rate of the master node along the i^{th} direction, q_i is described by

$$q_i = -k_{ij} \frac{\partial T}{\partial x_j} \quad (i, j = 1, 2) \quad (2)$$

where k_{ij} is the thermal conductivity tensor, and T is the temperature of the master node. For $\Delta 089$, the temperature is assumed to obey a linear distribution, and the heat flux will flow when the temperature of master node i is not identical to the remaining master nodes associated with slave nodes 8 and 9. Then, the temperature gradient of master node i can be kept as a constant by [19]

$$\frac{\partial T}{\partial x_i} = \frac{1}{A} \sum_{m=1}^3 \bar{T}^m \in_{ij} l_j^m \quad (3)$$

where A is the area of the triangle element, \bar{h}^m is the average temperature of edge m , l_j^m is the coordinate difference between the two nodes of edge m , and \in_{ij} is the two-dimensional matrix with

$$\in_{ij} = \begin{bmatrix} 0 & 1 \\ -1 & 0 \end{bmatrix} \quad (4)$$

Then, the heat flux into master node i induced by slave node 0 can be obtained by

$$Q_{i-0} = -\frac{q_i n_i^{(0)} L^{(0)}}{2} \quad (5)$$

where $n_i^{(0)}$ is the outer normal unit vector of the edge opposite to slave node 0, and $L^{(0)}$ denotes the length of the edge opposite to slave node 0. Similarly, the total heat flux of master node i contributed by its corresponding slave nodes is given by

$$Q_i = \sum_{m=0}^7 Q_{i-m} \quad (6)$$

where m is the number of slave nodes that belong to master node i . To align with the update of nodal displacements and velocities using the explicit time integration schemes (see Appendix A), we employ the finite difference method to explicitly update the nodal temperature within the updated heat flux, i.e.,

$$T^{\tau+\Delta t_h} - T^\tau = \frac{Q_i}{C_p M_s} \Delta t_h \quad (7)$$

Here

$$M_s = \sum_{k=0}^7 m_k \tag{8}$$

Δt_h is the thermal time step; $T^{t+\Delta t_h}$ and T^t denote the nodal temperature at the current and previous time instants, respectively; m_k is the mass of slave nodes (i.e., 0 to 7), and M_s is the mass of master node i . At the end of each iteration, the temperature of all slave nodes in the same group needs to be synchronized as the same as their master node, thereby achieving the continuum behavior of heat conduction in the intact/continuous deformation domain. To ensure the stability of the numerical model, the time step size of heat conduction should be less than the critical value specified as

$$\Delta t_h \leq \frac{L_{\min}^2}{4\kappa} \tag{9}$$

where L_{\min} is the minimum finite element size, and κ is the thermal diffusion coefficient ($\kappa = k/\rho C_p$ when $k_{ii} = k_{jj} = k$, ρ is the Bulk density).

Once a cohesive element is broken (i.e., a new microcrack is generated), the master–slave node mapping list related to the cohesive element needs to be updated accordingly. Such an update aims to ensure the independent computation of heat conduction of finite elements located in the same groups. Details on fracture initiation and propagation associated with cohesive elements can refer to Munjiza’s books [28,29] and previous works [22,30]. Continuing with the example shown in Fig. 1d-f and focusing on the master Nodes i and j , once the breakage of cohesive elements between Elements E_2 and E_3 occurs (see Fig. 1e), the connection between the slave nodes (e.g., Nodes 1 and 2) will be cut out, and the previous circle linked list becomes two open linked lists, e.g., $0 \rightarrow 1 \rightarrow 2$ and $3 \rightarrow 4 \rightarrow 5 \rightarrow 6 \rightarrow 7$ (Fig. 1f). Then, the slave Nodes 0 to 2 and 3 to 7 are automatically divided into two groups, which are respectively mapped to a new and old master node (e.g., i and j in Fig. 1e). Upon obtaining the updated master–slave list, the heat flux and nodal masses of slave nodes in each group are all accumulated to their master node. Therefore, using the node binding scheme, we can ensure the smooth transition of heat conduction from continuum to discontinuum during the solid fracturing process. Note that the other nodes of temperature update should also be processed at the same time in a similar manner.

2.2. Thermal contact model

Contact heat transfer occurs when an overlap area exists in two discrete bodies in touch or the fracture surfaces suffer from compressive loads (see Fig. 2a). For convenience, we take the contact pairs of ΔABC and ΔDEF (denoted as contactor triangle element β_c and the target triangle element β_t , respectively) as an example to illustrate the implementation of contact heat transfer (Fig. 2b). Based on the new energy-conserving contact model proposed in our previous work [31], we can obtain the heat flux between contact pairs through the overlap area ΔDGH , i.e.,

$$Q_{\text{con}} = h_c S_{\Delta DGH} (T_{c-M} - T_{t-M}) \tag{10}$$

where h_c is the thermal contact conductance coefficient; $S_{\Delta DGH}$ is the area of ΔDGH ; T_{c-M} and T_{t-M} are the temperatures of β_c and β_t at contact point M , respectively. Note that point M is the midpoint of edge GH in Fig. 2c. Then, we can distribute the contact heat flux (Q_{con}) to the six nodes of the contact pairs by

$$\begin{cases} Q_{\text{con}}^A = -N_A Q_{\text{con}} \\ Q_{\text{con}}^B = -N_B Q_{\text{con}} \\ Q_{\text{con}}^C = -N_C Q_{\text{con}} \end{cases} \tag{11}$$

and

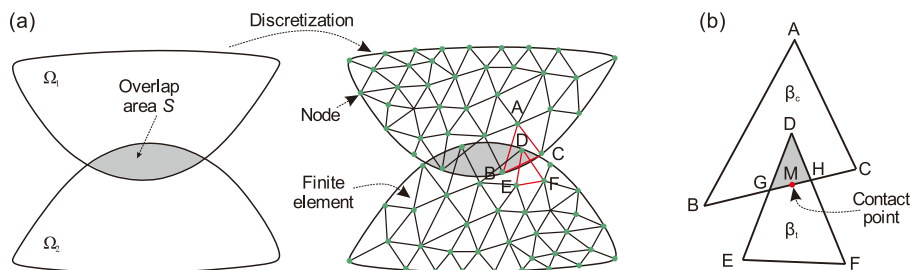


Fig. 2. (a) Discretization of discrete bodies in contact. (b) Contact heat transfer between two triangle elements in touch. The contactor triangle element and target triangle element are denoted as β_c and β_t , respectively. Ω_1 and Ω_2 denote two arbitrarily shaped bodies. Point M denotes the contact point where the total moment is zero.

$$\begin{cases} Q_{\text{con}}^{\text{D}} = N_{\text{D}}Q_{\text{con}} \\ Q_{\text{con}}^{\text{E}} = N_{\text{E}}Q_{\text{con}} \\ Q_{\text{con}}^{\text{F}} = N_{\text{F}}Q_{\text{con}} \end{cases} \quad (12)$$

where N_A, N_B, N_C, N_D, N_E and N_F are the shape functions satisfying $N_A + N_B + N_C = 1$ and $N_D + N_E + N_F = 1$. More about the shape functions are detailed in previous books [28,29]. In addition, the location of the contact point (e.g., point M) and the calculation of the overlap area (e.g., $S_{\Delta\text{DGH}}$) can be referred to in our previous work [31]. The updated contact heat fluxes of these slave nodes are assembled to their corresponding master node, and then incorporated into Eq. (7) to update the master node's temperature. We conduct a similar manner on the remaining contact pairs, and thus achieve the heat transfer simulation between arbitrarily shaped discrete bodies (e.g., Ω_1 and Ω_2 in Fig. 2a).

2.3. Thermal boundary conditions

In our proposed thermo-mechanical coupling model, appropriate arrangements of thermal boundary conditions are crucial to simulate heat transfer and thermal-induced cracking. Generally, the thermal boundary conditions involve three categories, i.e., Dirichlet (i.e., temperature), Neumann (i.e., heat flux), and Robin boundary conditions (see Fig. 3).

For the Dirichlet boundary condition, the given temperature ($T_1(t)$) is directly applied to the boundary nodes of a solid domain, i.e.,

$$T_{b1} = T_1(t) \quad (13)$$

where T_{b1} represents the temperature of a boundary node. For the Neumann boundary condition, a heat flux $q(t)$ is applied on the solid boundary. Then, the total heat flux (Q_{b2}) flows into the solid boundary can be expressed by

$$Q_{b2} = q(t)L \quad (14)$$

where L is the length of the solid boundary and the related boundary nodes (green dots in Fig. 3) participate in the temperature update according to Eq. (7). For the Robin boundary condition, the heat flux exchange will occur due to the temperature difference between the common boundaries of solid and fluid. Then, the heat flow into the solid contributed by high-temperature fluid is given by

$$Q_{b3} = h_{\text{ex}}(T_f - T_s) \quad (15)$$

where T_s and T_f represent the temperatures of solid and fluid, respectively; h_{ex} is the heat exchange coefficient between the fluid and solid. Related boundary nodes (red dots in Fig. 3) also participate in the temperature update.

2.4. Thermo-mechanical coupling

Based on the assumption of linear thermal expansion, the deformation gradient tensor \mathbf{F} can be decomposed into a thermal component \mathbf{F}_t and an elastic \mathbf{F}_e component using the multiplicative decomposition [25], i.e.,

$$\mathbf{F} = \mathbf{F}_t\mathbf{F}_e = (1 + \alpha\Delta T)\mathbf{F}_e \quad (16)$$

where α is the thermal expansion coefficient, and ΔT is the temperature change of a finite element that can be obtained by linearly interpolating the three nodal temperatures. The elastic \mathbf{F}_e component equals the deformation gradient tensor when the model only

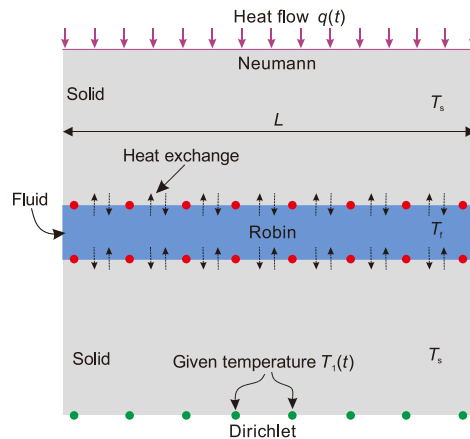


Fig. 3. Three different thermal boundary conditions, i.e., (a) Dirichlet (i.e., temperature), (b) Neumann (i.e., heat flux), and (c) Robin boundary conditions. T_s and T_f represent the temperatures of solid and fluid, respectively, and L is the length of the solid boundary.

considers the mechanical response [28]. To capture the stress and deformation distribution of a solid domain, we employ the Neo-Hookean elastic model to describe the mechanical behavior of constant strain finite elements. Then, the Cauchy stress tensor σ_{ij} considering thermal expansion can be given by

$$\sigma_{ij} = \frac{\lambda}{2} \left(J_t - \frac{1}{J_t} \right) \delta_{ij} + \frac{\xi}{J_t} (\mathbf{B}_{ij}^t - \delta_{ij}) + \eta \mathbf{D}_{ij}^t \quad (i, j = 1, 2) \tag{17}$$

Here

$$J_t = \det(\mathbf{F}) = \det(\mathbf{F}_t \mathbf{F}_e) = (1 + \alpha \Delta T)^2 \det(\mathbf{F}_e) \tag{18}$$

$$\mathbf{B}_{ij}^t = \mathbf{F}_t \mathbf{F}_e (\mathbf{F}_t \mathbf{F}_e)^T = (1 + \alpha \Delta T)^2 \mathbf{B}_{ij} \tag{19}$$

$$\eta = 2h\sqrt{E\rho} \tag{20}$$

and

$$\mathbf{D}_{ij}^t = \frac{1}{2} \left(\dot{\mathbf{F}}_t \mathbf{F}_t^{-1} + \left(\dot{\mathbf{F}}_t \mathbf{F}_t^{-1} \right)^T \right) + \mathbf{D}_{ij} = \frac{\alpha}{1 + \alpha \Delta T} \frac{\partial T}{\partial t} \mathbf{I} + \mathbf{D}_{ij} = \frac{\alpha \Delta T}{1 + \alpha \Delta T} \mathbf{I} + \mathbf{D}_{ij} \tag{21}$$

where λ and ξ are the Lamé constants, $\det(\cdot)$ is the determinant of solid matrix, \mathbf{B}_{ij} and \mathbf{D}_{ij} denote the left Cauchy-Green deformation and rate of deformation tensors, respectively, η is the viscous damping coefficient of finite element [32], h is the minimum finite element size, E is Young’s modulus, ρ is the bulk density, and δ_{ij} is the Kronecker delta. Then, Eq. (17) can be rewritten as

$$\sigma_{ij} = \frac{\lambda}{2} \left((1 + \alpha \Delta T)^2 \det(\mathbf{F}_e) - \frac{1}{(1 + \alpha \Delta T)^2 \det(\mathbf{F}_e)} \right) \delta_{ij} + \frac{\xi}{(1 + \alpha \Delta T)^2 \det(\mathbf{F}_e)} \left((1 + \alpha \Delta T)^2 \mathbf{B}_{ij} - 1 \right) + \eta \left(\frac{\alpha \Delta T}{1 + \alpha \Delta T} \delta_{ij} + \mathbf{D}_{ij} \right) \tag{22}$$

Compared with previous thermo-mechanical models [17,23], our proposed approach has the capability of considering the large deformation and rotations induced by temperatures, which aligns with the finite strain framework in FDEM. The simulation workflow of the thermo-mechanical coupling model is summarized in Fig. 4. The thermal solver model mainly involves heat conduction of a triangle element and heat transfer of discrete bodies or fracture surfaces. The updated nodal temperature would yield the variance of thermal stress, thereby producing the mechanical response of the solid domain (Eq. (22)). Once local stresses meet the strength criteria (i.e., the breakage of cohesive elements occurs), we need to update the master–slave lists related to heat nodes to realize temperature discontinuity at the two sides of a fracture. The mechanical solver consists of the calculation of finite elements, cohesive elements and contact interaction. At the end of each iteration, we employ the explicit time integration scheme to update nodal displacements and velocities based on Newton’s second law (see Appendix A). Each physical solver has a corresponding critical time step, which must guarantee the numerical stability of the numerical model (Eq. (9)). Calculation of solid time step (Δt_s) related to mechanical solver can refer to the previous works [27,31]. Upon this process, we can achieve the thermo-mechanical coupling model in FDEM. More benchmark examples are conducted in the next section to verify the accuracy and robustness of the proposed thermo-mechanical coupling model.

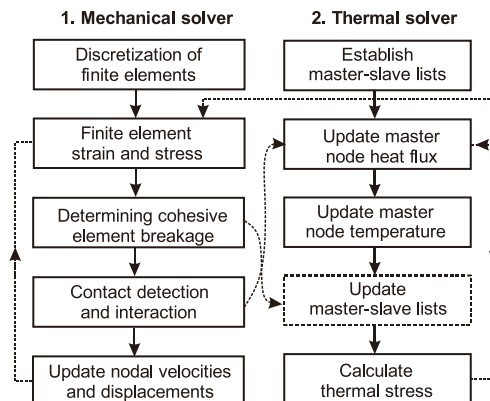


Fig. 4. Simulation workflow of thermo-mechanical coupling model.

3. Model verification and comparison

In this section, we conduct several benchmark examples to verify the accuracy and robustness of the proposed thermo-mechanical coupling model in terms of heat conduction, thermal cracking and heat transfer within the current framework of FDEM. Then, the computational efficiency of the proposed approach compared with the widely used approach is also demonstrated. For simplicity, we define the variable R_{ero} as the maximum relative errors between the FDEM simulated results and the analytical solution and then are divided by the analytical solution for all numerical cases. We note that the sign convention of tension as positive is used for all numerical cases.

3.1. Heat conduction

We benchmark two examples to verify the robustness and accuracy of the proposed approach in terms of steady-state and transient heat conduction against the theoretical solutions in this section. In addition, the mesh sensitivity analysis for heat conduction is conducted in Appendix B, verifying that the mesh size used in this section can avoid the mesh size dependency problem.

3.1.1. Steady-state heat conduction in hollow disc

In this case, we establish a thick-wall disc with inner radius $r_i = 0.5$ m and outer radius $r_o = 5$ m (Fig. 5a) to verify the accuracy of heat conduction and thermo-mechanical coupled response under a steady state. The disc is assumed to be homogeneous, isotropic and elastic. We apply the fixed temperature at T_i (100 °C) and T_o (10 °C) on the inner and outer boundaries of the disc, respectively. The analytical solution for the temperature distribution in the thick-walled disc along the radial direction (i.e., monitoring line in Fig. 5a) under a steady state is given by [33]

$$T = \frac{\ln\left(\frac{r_o}{r}\right)}{\ln\left(\frac{r_o}{r_i}\right)} T_i + \frac{\ln\left(\frac{r_i}{r}\right)}{\ln\left(\frac{r_o}{r_i}\right)} T_o \quad (23)$$

According to the thermo-elasticity theory, the radial and tangential thermal stresses for plane strain problems induced by temperature change are calculated by [34]

$$\sigma_r = \frac{\alpha E}{2(1-\nu)} (T_i - T_o) \left(\frac{\ln(r_o/r)}{\ln(r_o/r_i)} - \frac{r_o^2/r^2 - 1}{r_o^2/r_i^2 - 1} \right) \quad (24)$$

and

$$\sigma_\theta = \frac{\alpha E}{2(1-\nu)} (T_i - T_o) \left(\frac{\ln(r_o/r)}{\ln(r_o/r_i)} + \frac{r_o^2/r^2 + 1}{r_o^2/r_i^2 - 1} \right) \quad (25)$$

where r is the distance from a temperature monitor point to the center of the disc, σ_r and σ_θ are the radial and tangential stress, respectively, α is the thermal expansion coefficient, E is Young's modulus, and ν is Poisson's ratio. The model input parameters are tabulated in Table 1. The model consists of 20,181 triangle elements with an average element size of 0.1 m, and the total simulation time is 4.6 s. Note that we adopt $\eta = 2h\sqrt{E\rho}$ (see Eq. (20)) to calculate the viscous damping coefficient of finite elements for all numerical cases [32].

The final temperature distribution in the thick-wall disc is shown in Fig. 5b. The temperature gradually decreases from inside to outside, and the temperatures at monitoring points with the same distance to the center of the thick-wall disc are equal. As shown in Fig. 5c, the maximum relative errors, R_{ero} (as defined earlier), with respect to temperature distribution along the monitoring line are

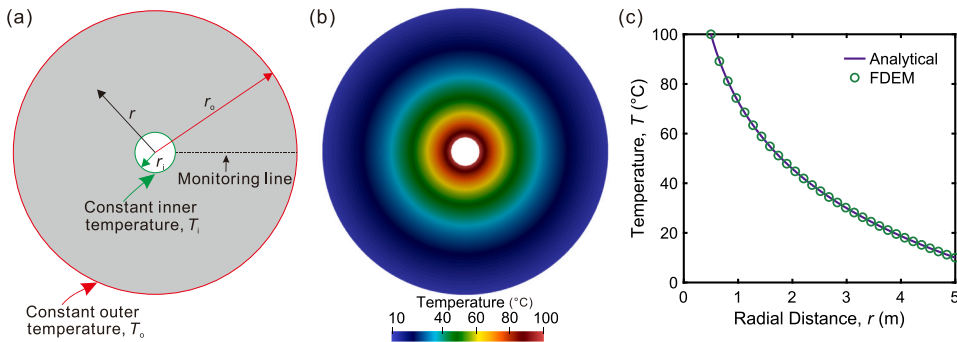


Fig. 5. Steady-state radial heat conduction in the disc. (a) Geometry and boundary conditions of the model. (b) Temperature distribution in the disc. (c) Comparison between analytical and FDEM-simulated radial temperature distribution.

Table 1
Input parameters in FDEM simulations for the steady-state heat conduction.

Input parameters	Values
Young's modulus, E (GPa)	30
Bulk density, ρ (kg/m ³)	2550
Poisson's ratio, ν	0.2
Viscous damping coefficient, η (kg/m-s)	7×10^5
Normal contact penalty, P_n (GPa)	300
Tangential contact penalty, P_t (GPa)	300
Thermal conductivity coefficient, k (W/(m·°C))	200
Heat capacity, C_p (J/(kg·°C))	8
Thermal expansion coefficient α , (1/°C)	3.0×10^{-6}
Solid time step Δt_s , (s)	2.3×10^{-6}
Thermal time step Δt_h , (s)	2.0×10^{-5}

merely 2.1×10^{-4} . Such minor relative errors verify the accuracy of the proposed approach for heat conduction simulation in elastic media. The numerical results of the radial and tangential stress profiles along the radius are shown in Fig. 6. We can observe that the radial stress gradually decreases from inside to outside, whereas the tangential stress increases first and then decreases. The stress distribution obtained from the FDEM simulation is consistent with the analytical solution, and the maximum relative errors (R_{ero}) for the radial and tangential stress are only 3.2 % and 1.2 %, respectively, demonstrating the capability of our proposed approach for thermo-mechanical coupling simulation.

3.1.2. Temperature distribution in transient states

In this case, we construct a rectangular plate with dimensions of 1 m × 0.25 m (length × width) to verify the accuracy of heat conduction in a transient state. The left and right boundaries of the plate are exposed to two constant temperatures of T_L (0 °C) and T_R (100 °C), respectively, whereas its bottom and top boundaries are adiabatic. The model consists of 4,556 triangle elements with an average element size of 30 mm (see Fig. 7a), and the input parameters are tabulated in Table 2. Note that a horizontal monitoring line marked in blue with $y = 0$ is set in the model center to measure the temperature and stress evolution via time. The analytical solution for temperature is a function of x (distance from the left boundary) and t (time) [35], i.e.,

$$T(x, t) = T_L + (T_R - T_L) \frac{x}{l} + \frac{2}{\pi} \sum_{n=1}^{\infty} \frac{T_R \cos n\pi - T_L}{n} \sin \frac{n\pi x}{l} \exp(-\kappa n^2 \pi^2 t / l^2) + \frac{4T}{\pi} \sum_{m=0}^{\infty} \frac{1}{2m+1} \sin \frac{(2m+1)\pi x}{l} \exp(-\kappa(2m+1)^2 \pi^2 t / l^2) \tag{26}$$

Here

$$\kappa = k / (\rho C_p) \tag{27}$$

where T is the initial temperature of the model (zero in this case), κ is the thermal diffusivity, k is thermal conductivity, l is the length of a rectangular plate, ρ is the bulk density, and C_p is the specific heat.

Based on the distribution of temperature, the thermally induced stresses for the plane strain problem can be obtained by

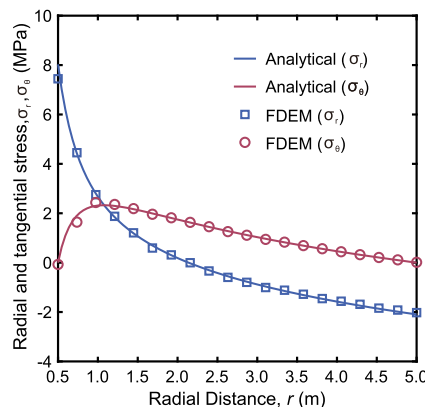


Fig. 6. Comparison between analytical and FDEM-simulated results for stress distribution along radial and tangential directions.

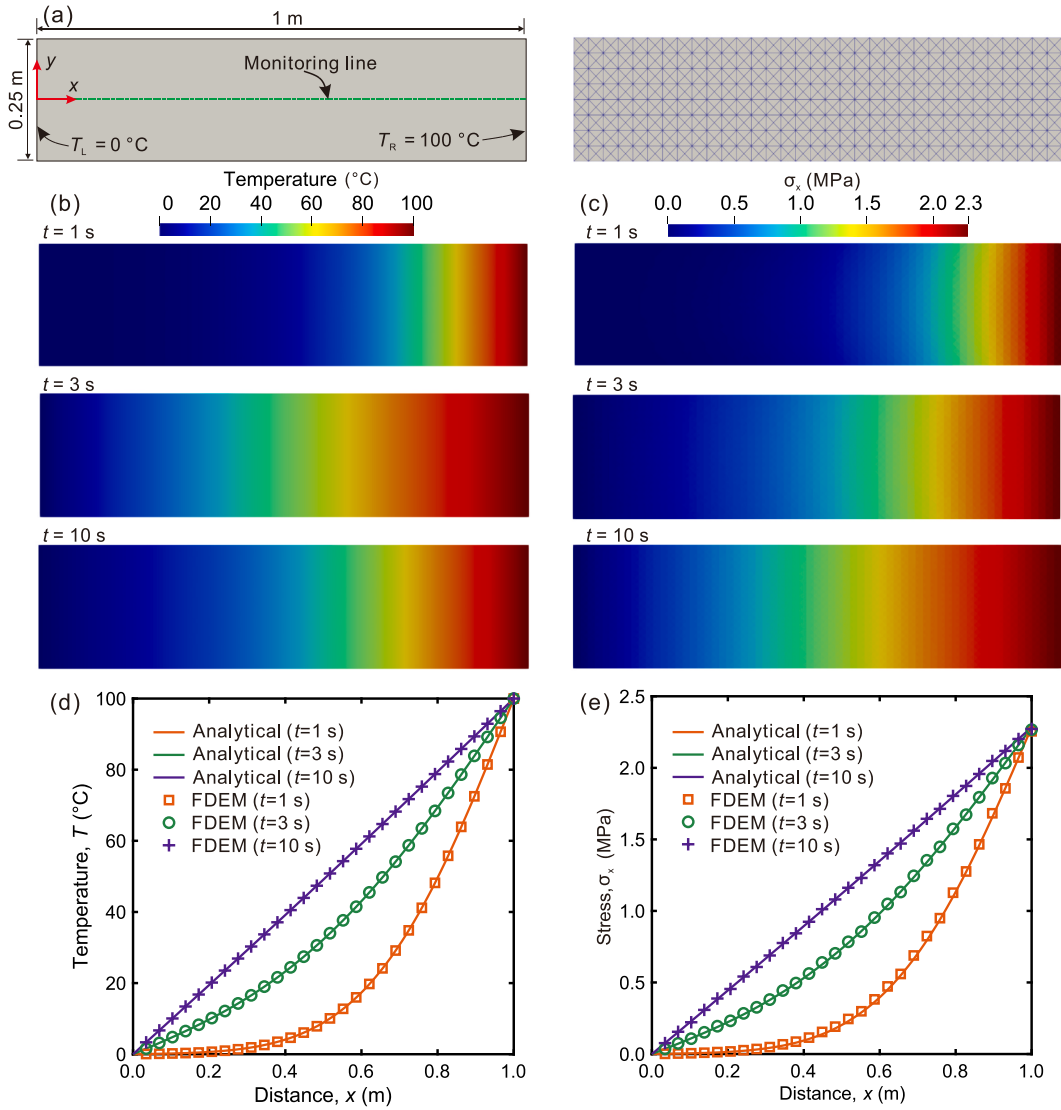


Fig. 7. (a) Model geometry and mesh (the dotted line is the monitoring line). (b) Temperature distribution at three timestamps: 1 s, 3 s and 10 s. (c) Thermal stress distribution along x direction at three timestamps: 1 s, 3 s and 10 s. Comparison between analytical and FDEM results for (d) temperature and (e) stress distribution along the monitoring line.

Table 2

Input parameters in FDEM simulations for the uniformly heated plate.

Input parameters	Values
Young's modulus, E (GPa)	30
Bulk density, ρ (kg/m^3)	2700
Poisson's ratio, ν	0.27
Viscous damping coefficient, η ($\text{kg}/\text{m}\cdot\text{s}$)	2.7×10^5
Normal contact penalty, P_n (GPa)	300
Tangential contact penalty, P_s (GPa)	300
Sample friction coefficient, μ (-)	0.7
Thermal conductivity coefficient, k ($\text{W}/(\text{m}\cdot^\circ\text{C})$)	210
Heat capacity, C_p ($\text{J}/(\text{kg}\cdot^\circ\text{C})$)	1.8
Thermal expansion coefficient α , ($1/^\circ\text{C}$)	3.5×10^{-7}
Solid time step Δt_s , (s)	4.0×10^{-7}
Thermal time step Δt_h , (s)	1.0×10^{-6}

$$\sigma_x = \sigma_y = -\frac{E}{1-2\nu}\alpha[T(x,t) - T'] \tag{28}$$

where E is Young's modulus, ν is the Poisson's ratio, α is the thermal expansion coefficient, σ_x and σ_y denote the components of thermal stresses along x and y axis directions, respectively. The temperature distribution at three timestamps (1 s, 3 s and 10 s) are presented in Fig. 7b & d. It can be observed that the temperature gradually increases from the left to the right side of the plate, and the maximum relative errors (R_{ero}) for temperature distribution at three timestamps are merely are only 1.26×10^{-5} . Such minor relative errors demonstrate the correctness of heat conduction in a transient state using our proposed approach. For convenience, we only record the stress evolution along the x direction (σ_x) on the monitoring line. As shown in Fig. 7c & e, we find excellent agreement between FDEM simulation and analytical solution in terms of the stress distribution along the horizontal monitoring line. The maximum relative errors (R_{ero}) for stress distribution at three timestamps are only 3.52×10^{-5} , which further verifies the accuracy of our proposed approach in simulating the thermo-mechanical response with respect to heat conduction under a transient state.

3.2. Thermal cracking

In this section, three examples are employed to demonstrate the capability of our proposed approach to simulate thermal cracking. The selected mesh size in this section can avoid the mesh dependency on solid fracturing simulation induced by thermal shock. More details and analysis on the mesh sensitivity of solid fracturing are presented in Appendix C.

3.2.1. Thermal cracking of disc-ring

The radius of the inner disc and outer ring are 8 mm and 38 mm (see Fig. 8a), respectively. The initial temperature of the model is set to 20 °C (room temperature), then the model temperature increases uniformly from 20 °C to 100 °C and then remains unchanged. The model consists of 20,464 triangle elements with an average element size of 3.8 mm, and the input parameters are tabulated in Table 3. Note that the thermal expansion coefficient of the inner disc is larger than that of the outer ring, and thus produces thermal stress due to the inconsistent deformation between them. As the temperature increases, the inner disc bears compression while the inner boundary of the outer ring is subjected to tensile expansion. Prior to fracturing, for the plane stress problem, the analytical solutions of the radial stress σ_r and tangential stress σ_θ of the disc and ring along the monitoring line (i.e., red dotted line in Fig. 8a) can be respectively obtained by [36]

$$\sigma_r = \begin{cases} -\varepsilon\Delta T & r \leq r_i \\ -\frac{r_i^2(r_o^2 - r^2)}{r^2(r_o^2 - r_i^2)}\varepsilon\Delta T & r_i < r \leq r_o \end{cases} \tag{29}$$

and

$$\sigma_\theta = \begin{cases} -\varepsilon\Delta T & r \leq r_i \\ \frac{r_i^2(r_o^2 + r^2)}{r^2(r_o^2 - r_i^2)}\varepsilon\Delta T & r_i < r \leq r_o \end{cases} \tag{30}$$

where r is the distance from the center; r_o and r_i are the radius of the outer ring and inner disc; ΔT is the temperature variance of the model; ε is the strain represented by

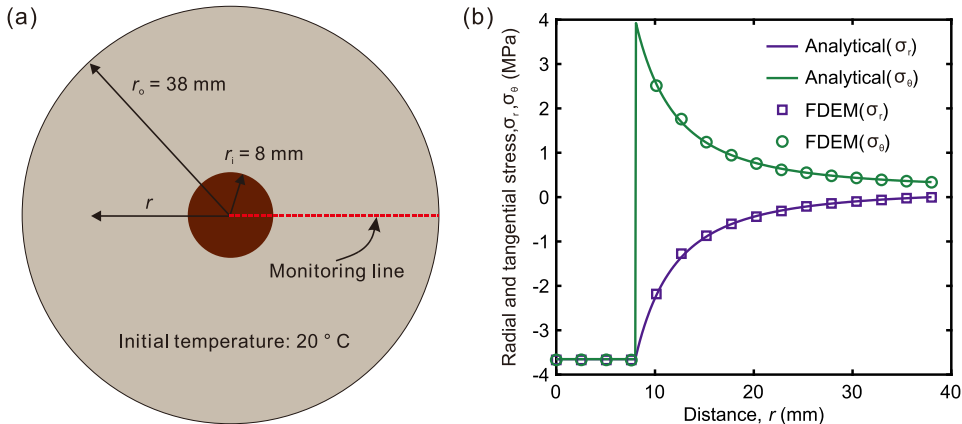


Fig. 8. (a) Model geometry (the monitoring line is marked by the red dotted line). (b) Analytical and numerical results of radial stress σ_r and tangential stress σ_θ of the disc-ring model at $\Delta T = 20$ °C. (For interpretation of the references to colour in this figure legend, the reader is referred to the web version of this article.)

Table 3
Input parameters in FDEM simulations for disc-ring model [16,17].

Input parameters	Disc	Ring
Young's modulus, E (GPa)	40	20
Bulk density, ρ (kg/m ³)	2300	2300
Poisson's ratio, ν	0.3	0.2
Tensile strength, f_t (MPa)	10	4.5
Cohesion, c (MPa)	20	20
Mode I fracture energy, G_{I1} (J/m ²)	4	2
Mode II fracture energy, G_{I2} (J/m ²)	20	10
Viscous damping coefficient, η (kg/m·s)	4700	2600
Normal contact penalty, P_n (GPa)	400	200
Tangential contact penalty, P_s (GPa)	400	200
Sample friction coefficient, μ (–)	0.7	0.7
Thermal conductivity coefficient, k (W/(m·°C))	1.2	1.2
Heat capacity, C_p (J/(kg·°C))	900	900
Thermal expansion coefficient α , (1/°C)	2.2×10^{-5}	7.0×10^{-6}
Solid time step Δt_s , (s)	1.5×10^{-8}	1.5×10^{-8}
Thermal time step Δt_h , (s)	3.0×10^{-7}	3.0×10^{-7}

$$\varepsilon = \frac{\alpha_1 - \alpha_2}{p} \quad (31)$$

and α_1 and α_2 are the linear thermal expansion coefficients of the disc and ring, respectively; p can be obtained by

$$p = \frac{1 - \nu_1}{E_1} + \frac{(r_o^2 + r_i^2) + \nu_2(r_o^2 - r_i^2)}{E_2(r_o^2 - r_i^2)} \quad (32)$$

and E_1 and E_2 are Young's modulus of the disc and ring, respectively; ν_1 and ν_2 are the Poisson's ratio of the disc and ring, respectively.

The radial and tangential stress along the monitoring line (see the red dotted line in Fig. 8a) at $\Delta T = 20^\circ\text{C}$ are presented in Fig. 8b. We can observe that the radial and tangential stresses of the outer ring gradually decrease and increase with the increasing distance from monitoring points to the model center, respectively, whereas the stress components of the inner disc are equal. The maximum relative errors (R_{ero}) in terms of the stress distribution in the disc-ring model are only 2.9×10^{-4} , verifying the accuracy of our proposed approach in capturing the thermo-mechanical response with different thermal expansion coefficients. As the temperature further increases, the tensile stress of the outer ring at $r = 8$ mm will reach the tensile strength, thereby inducing fracture initiation and propagation. Fig. 9a-b presents the fracture propagation patterns with various temperatures induced by thermal stress. When temperature increases to 60°C ($\Delta T = 40^\circ\text{C}$), two fractures are initiated from the inner boundary of the ring and propagate towards the outer boundary. Finally, three fractures featured with symmetrical locations are observed in the outer ring at $\Delta T = 80^\circ\text{C}$. The simulated fracture propagation patterns are similar to the experimental observations (see Fig. 9c), which exhibits the capability of our proposed approach to simulate thermal cracking induced by various thermal expansion coefficients.

3.2.2. Thermal cracking in disc

We select the circular specimen with a diameter of 13 mm to simulate the thermal shock progress (see Fig. 10b). According to the previous experiment (see Fig. 10a), the thin circular ceramic plates, composed of 99% Al_2O_3 , are tightly stacked together in four sets, with two thick circular plates on the outside. The model consists of 15,352 triangle elements with an average element size of 4 mm (Fig. 10c), and the input parameters are tabulated in Table 4. Five different initial temperatures for the circular ceramic specimen are adopted in this case: 250°C , 300°C , 350°C , 400°C and 500°C . Then, the heated ceramic specimen is placed into water at a constant temperature of 20°C . Fig. 11a presents the final thermal shock fracture patterns obtained by FDEM simulation at different initial

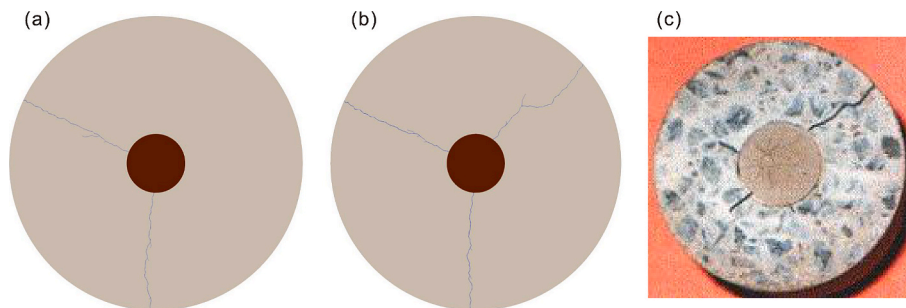


Fig. 9. The thermal crack propagation pattern at increasing temperature intervals: (a) $\Delta T = 40^\circ\text{C}$ and (b) $\Delta T = 80^\circ\text{C}$. (c) Thermal cracking geometry in the laboratory ($\Delta T = 80^\circ\text{C}$) [37].

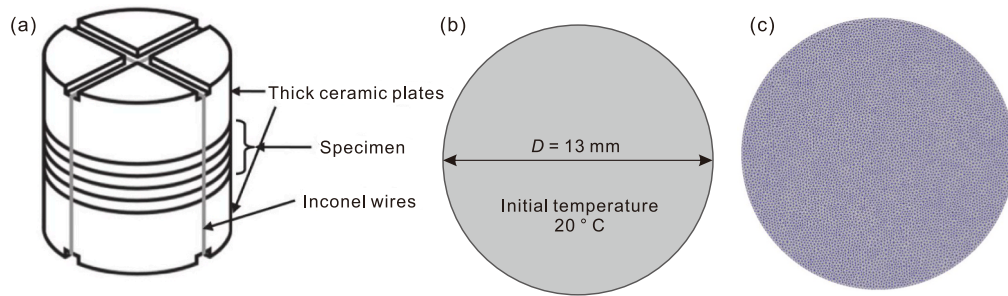


Fig. 10. (a) Bound specimens for thermal shock [38]. (b) Specimen geometry. (c) Mesh.

Table 4

Input parameters of the disc for thermal cracking simulation [23].

Input parameters	Value
Young's modulus, E (GPa)	370
Bulk density, ρ (kg/m^3)	3980
Poisson's ratio, ν	0.33
Tensile strength, f_t (MPa)	180
Cohesion, c (MPa)	200
Mode I fracture energy, G_{I1} (J/m^2)	12.16
Mode II fracture energy, G_{I2} (J/m^2)	24.32
Viscous damping coefficient, η ($\text{kg}/\text{m}\cdot\text{s}$)	5000
Normal contact penalty, P_n (GPa)	3700
Tangential contact penalty, P_s (GPa)	3700
Sample friction coefficient, μ (-)	0.7
Thermal conductivity coefficient, k ($\text{W}/(\text{m}\cdot^\circ\text{C})$)	35
Heat capacity, C_p ($\text{J}/(\text{kg}\cdot^\circ\text{C})$)	900
Thermal expansion coefficient α , ($^\circ\text{C}$)	9.5×10^{-5}
Solid time step Δt_s , (s)	1.2×10^{-9}
Thermal time step Δt_h , (s)	2.0×10^{-7}

temperatures. We can observe that the thermal shock cracks, as typical tensile cracks, are all initiated from the specimen's outer boundary and propagate towards the center. Besides, the crack spacing and length exhibit obvious hierarchical characteristics, and most cracks will stop propagation. With the increasing initial temperature of the circular specimen, the crack length and number also increase, and similar observations have been reported in previous simulations [8] and experiments [38] (see Fig. 11b-c). The comparison of crack number and length between simulations and experiments is shown in Fig. 11d-f. We can observe that both the crack number and crack length increase with the increment of the initial temperature, and the simulated results exhibit a good trend with the experiments [23]. In addition, the crack number obtained from experimental observation is generally less than that of simulations, which arises from the absence of observing some microcracks in the experiments.

3.2.3. Thermal cracking of Lac du Bonnet granite specimen

In this case, a Lac du Bonnet (LdB) granite specimen with a borehole is adopted to simulate the thermal cracking process (see Fig. 12a), where the inner radius of a borehole and the outer radius of the granite specimen are 1.5 mm and 15 mm, respectively. The initial temperature of the granite specimen is 20°C . We place the heat source rod inside the borehole to heat the granite specimen, thereby applying a constant heat source with $1.5 \times 10^6 \text{ W}/(\text{m}^2\cdot^\circ\text{C})$ on its inner boundary (Neumann boundary condition illustrated in Section 2.3). The model consists of 20,181 triangle elements with an average element size of 0.3 mm, and the input parameters used in this model are shown in Table 5. The fracture patterns and temperature evolution at two timestamps ($t = 0.5 \text{ s}$ and 1 s) are presented in Fig. 13. It can be observed that the fracture is first initiated from the outer boundary of the granite ($t = 0.5 \text{ s}$), while the temperature distribution is not affected by the crack generation. As the temperature increases ($t = 1 \text{ s}$), the fracture propagates towards the model center until it reaches the granite specimen's inner boundary, forming a macroscopic fracture plane. Furthermore, a discontinuous temperature distribution is observed on the two sides of the fracture, demonstrating that the macroscopic fracture can restrict the flow of heat fluxes in this case. The thermal cracking patterns of the LdB granite specimen obtained from FDEM results are in good agreement with the previous experimental observations [39] and numerical simulations (i.e., the peridynamic and PFC numerical results) [40,41] (see Fig. 14b-d), which demonstrates the capability of the proposed approach for thermal cracking simulation.

3.3. Contact heat transfer

In this section, we first verify the accuracy of the contact heat transfer model, and then demonstrate its capability of capturing the temperature evolution in granular particles.

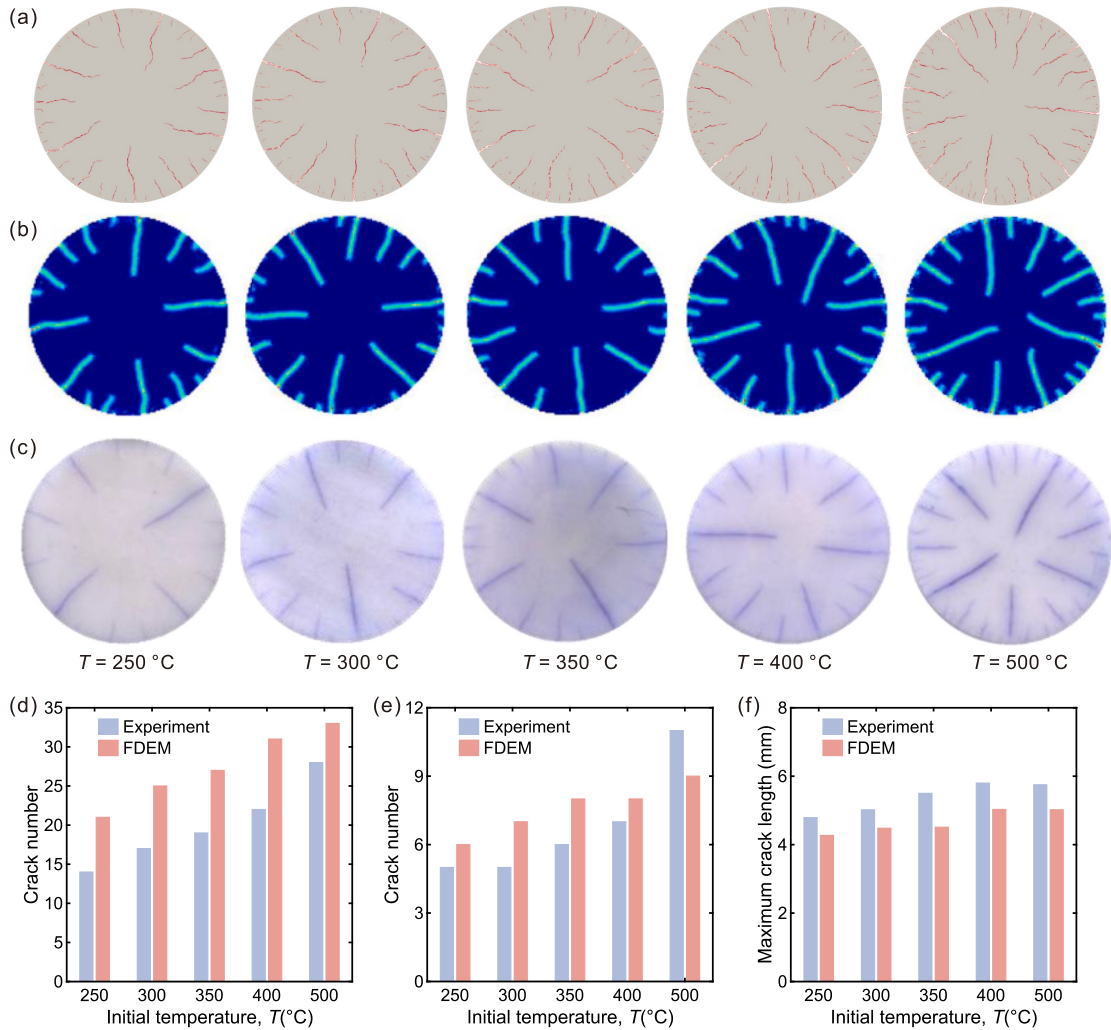


Fig. 11. Comparison of the final thermal shock crack patterns at different initial temperatures. (a) The current FDEM results. (b) The peridynamic numerical results [8]. (c) The experimental results [38]. Comparison of (d) total crack number, (e) long crack number, and (f) maximum crack length between simulations and experiments [23].

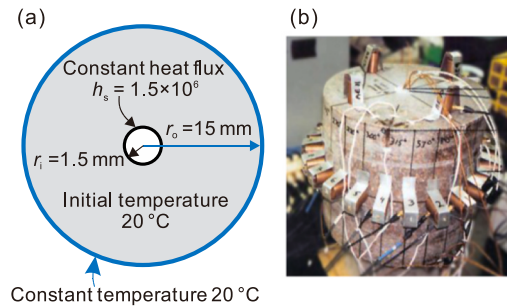


Fig. 12. Geometrical and thermal loading conditions of the LdB granite specimen during the heated experiment [40].

3.3.1. Contact heat transfer between discrete blocks

The model of contact heat transfer between three square blocks is shown in Fig. 15a. Each square block has an edge length of 100 mm, and they are stacked with a total model length of 300 mm. To guarantee each block transfers heat flux through contact overlap, a pressure of 1.0 MPa is applied on the top of the top block to ensure contact between them. The displacements of the bottom boundary of

Table 5
Physical properties of LdB granite specimens with a borehole [23,40].

Input parameters	Value
Young's modulus, E (GPa)	67
Bulk density, ρ (kg/m ³)	2650
Poisson's ratio, ν	0.33
Tensile strength, f_t (MPa)	1.5
Cohesion, c (MPa)	20
Mode I fracture energy, G_{I1} (J/m ²)	2
Mode II fracture energy, G_{I2} (J/m ²)	10
Viscous damping coefficient, η (kg/m·s)	3200
Normal contact penalty, P_n (GPa)	670
Tangential contact penalty, P_t (GPa)	670
Sample friction coefficient, μ (-)	0.7
Thermal conductivity coefficient, k (W/(m·°C))	60
Heat capacity, C_p (J/(kg·°C))	300
Thermal expansion coefficient α , (1/°C)	3.5×10^{-6}
Solid time step Δt_s , (s)	4.0×10^{-9}
Thermal time step Δt_h , (s)	4.0×10^{-6}

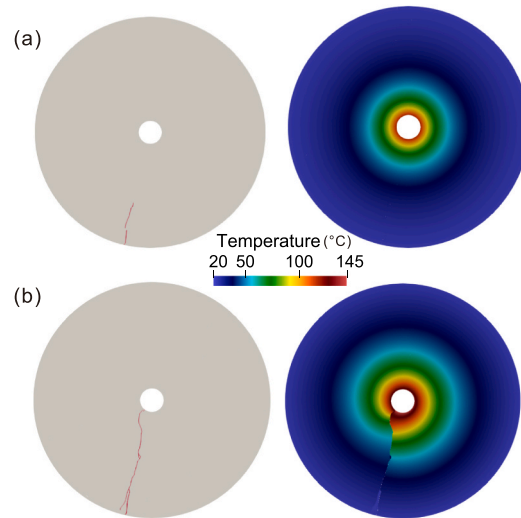


Fig. 13. Thermal-induced fracturing process of the LdB granite specimen at two timestamps: (a) 0.5 s and (b) 1 s.

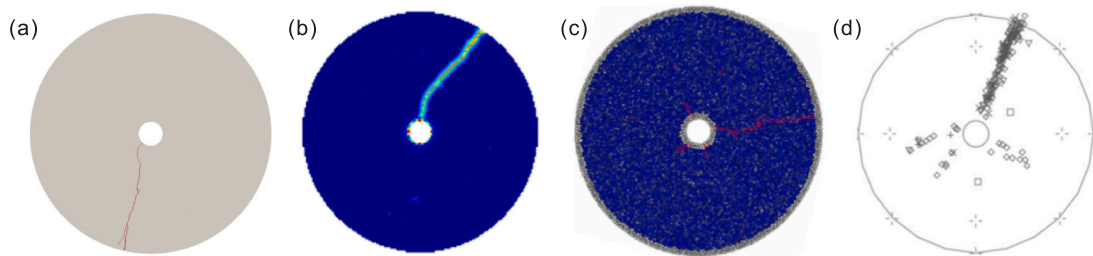


Fig. 14. Comparison of the ultimate failure patterns in the rock cylindrical specimen among (a) the proposed FDEM results, (b) the peridynamic numerical results [40], (c) the PFC (Particle Flow Code) simulation results [41] and (d) the previous experimental observations [39].

the model are fixed. The left and right boundaries of the model are adiabatic, whereas the temperature of the top and bottom boundaries of the model are fixed at T_1 (100 °C) and T_2 (0 °C), respectively. The parameters used for this model are tabulated in Table 6. The model consists of 84 triangle elements with an average element size of 30 mm, and the effect of thermal expansion is not considered in this case.

As presented in Fig. 15b-d, we can observe that the discontinuous temperature is encountered between two block boundaries due to the thermal resistance of contact heat transfer. The temperature distribution tends to be uniform in the model when the heat transfer

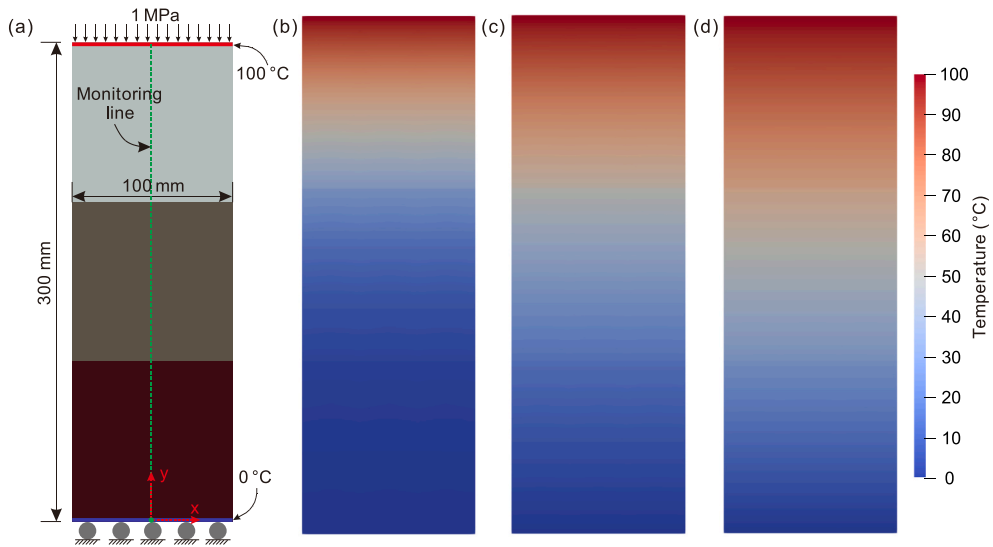


Fig. 15. Temperature distribution at various timestamps (2 s, 5 s and 10 s). (a) Model geometry (the monitoring line is marked by a green dotted line). (b) $t = 2$ s. (c) $t = 5$ s. (d) $t = 10$ s. (For interpretation of the references to colour in this figure legend, the reader is referred to the web version of this article.)

Table 6

Input parameters for the three blocks for contact heat transfer simulation.

Input parameters	Value
Young's modulus, E (GPa)	30
Bulk density, ρ (kg/m^3)	2700
Poisson's ratio, ν	0.27
Viscous damping coefficient, η ($\text{kg}/\text{m}\cdot\text{s}$)	3.0×10^5
Normal contact penalty, P_n (GPa)	300
Tangential contact penalty, P_s (GPa)	300
Thermal conductivity coefficient, k ($\text{W}/(\text{m}\cdot^\circ\text{C})$)	500
Heat capacity, C_p ($\text{J}/(\text{kg}\cdot^\circ\text{C})$)	80
Contact conductance coefficient, h_c , ($\text{W}/(\text{m}^2 \cdot ^\circ\text{C})$)	8.0×10^4
Solid time step Δt_s , (s)	1.0×10^{-7}
Thermal time step Δt_h , (s)	5.0×10^{-7}

reaches a steady state (see Fig. 15d). The analytical solution for temperature distribution along the monitoring line (see Fig. 15a) with time can refer to Eq. (26). Then, the comparison between the analytical solution and FDEM simulation for temperature distribution in terms of contact heat conduction at different timestamps ($t = 2$ s, 5 s and 10 s) is shown in Fig. 16. The temperature distribution obtained from the numerical simulation is consistent with the analytical solution along monitoring lines located inside the blocks.

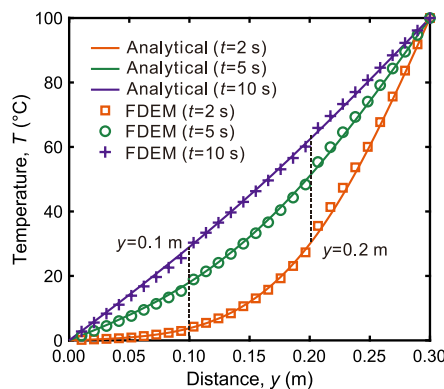


Fig. 16. Comparison between the analytical solution and the FDEM simulation in terms of temperature distribution at three timestamps ($t = 2$ s, 5 s and 10 s). The boundaries (i.e., $y = 0.1$ m and 0.2 m) between adjacent blocks are marked by black vertical dashed lines.

However, for the boundaries between adjacent blocks (i.e., $y = 0.1$ m and 0.2 m), the maximum relative errors (R_{ero}) for temperature distribution at three timestamps is $\sim 10.7\%$, which is caused by the difference between the thermal contact heat model and the heat conduction model.

3.3.2. Heat transfer in granular assembly

A model with an assembly of granular particles placed in a barrel is created to simulate heat transfer in granular particles. The barrel has dimensions of 400 mm \times 600 mm (width \times height), and the size of granular particles varies uniformly from 15 to 20 mm. The temperature of the barrel bottom remains constant at 200 °C, and the initial temperature of the granular particles is set to 25 °C. The particles contact each other under gravity with gravitational acceleration $g = -9.8$ m/s², and the barrel is fixed during the simulation. To ensure faster contact interaction among these particles, a constant pressure of 20 MPa is applied on the plate located on the upper side of the granular assembly. The parameters used for this model are tabulated in Table 7. The model consists of $32,048$ triangle elements with an average element size of 1.5 mm, and the mechanical response induced by thermal expansion is not considered. The evolution of temperature distribution in the granular assembly is presented in Fig. 17b-f. It can be observed that the temperature of the particles gradually increases from the bottom to the top of the barrel, which is consistent with the previous simulation [19].

3.4. Computational efficiency

As mentioned earlier, in order to approximate continuous heat conduction between adjacent finite element pairs, a large heat exchange coefficient (h_j) for cohesive elements has to be used in previous works [18,23,24]. In these traditional thermo-mechanical coupling models, a heat exchange coefficient that is too large can significantly increase the computational cost. Therefore, Yan and Jiao [23] defined $h_j = nk/L_{\text{min}}$ (n denotes the amplification factor, k is the thermal conductivity coefficient, and L_{min} is the minimum element size) to reach a relative balance between computational efficiency and numerical accuracy. They suggested using an amplification factor of 100 to achieve decent results for the discrete heat transfer model. For easy reference, this heat conduction model is named as the ‘original approach’ hereafter. It is worth noting that FDEM essentially reduces to the standard FEM in the absence of cracks or other discontinuities. To compare the computational efficiency between the proposed approach, the standard FEM and the original approach, we establish a rectangular plate with dimensions of 2 m \times 0.2 m (length \times width) to simulate the process of solid heat conduction (Fig. 18a). The left and right boundaries of the plate are exposed to two constant temperatures of T_L (0 °C) and T_R (100 °C), respectively; whereas its bottom and top boundaries are adiabatic. All simulations are carried out on the same hardware platform, i.e., an Intel Core i7-12700H CPU @ 2.90 GHz with 32 GB of RAM.

For convenience, we define a variable r_{effi} to denote the ratio of the computing time needed between the original and proposed approaches, as well as the standard FEM, upon heat conduction reaching a steady state. The width of the plate and average element size are denoted as L and h , respectively. The input thermal time step sizes under various mesh sizes are tabulated in Table 8. As shown in Fig. 18b, with the increase of L/h , i.e., a decrease of element size and thus an increase in the number of finite elements, the efficiency index r_{effi} increases nearly exponentially and reaches around 110 times when $L/h = 80$ (about $2,560$ triangle elements). Therefore, heat conduction implemented in our proposed approach can effectively reduce computational cost in the intact/continuous deformation domain compared with the original approach [18,23,24]. In addition, compared with the standard FEM, the computational efficiency of our proposed approach slightly decreases, which mainly arises from the establishment and implementation of node binding lists. Moreover, we need to assemble the nodal mass of slave nodes to its corresponding master node (see Eq. (8)), which further reduces the computational efficiency. Furthermore, the temperature distribution at various steps (600 , $1,500$ and $3,000$ steps) when $L/h = 20$ is presented in Fig. 19. We can observe that the heat conduction has reached a steady state with $3,000$ steps using the proposed approach, while the heat flux mainly distributes on the right side of the plate when the original approach is adopted. Obviously, the heat conduction speed of the proposed approach is faster than that of the original approach, which also demonstrates the improved computational efficiency of the proposed approach in terms of solid heat conduction.

4. Application example

With the development of deep underground resource exploitation, granite formations, a significant natural geological barrier, are often exposed to high-temperature environments. However, due to the complexity of mineral grain structures and spatial distribution of pre-existing fractures, granite features a strong geometric heterogeneity on the micro-scale. In addition, the initiation and propagation of thermal cracks are highly dependent on the thermal expansion coefficient of minerals. Here, a granite sample with dimensions of 25 mm \times 25 mm (width \times height) is established to consider the coupled response of thermo-mechanical fields (Fig. 20a), which aims to investigate the micro-mechanisms of thermal cracks of crystalline rocks. We adopt the open-source Neper software (Version 4.5.1) to construct a grain-based model (GBM) [42] for representing the micro-heterogeneity of granite, where each mineral is featured with the polygonal grain (Fig. 20a). After constructing the model, the regularization method is employed in Neper to remove small edges and faces and improve mesh quality, and thus avoid small simulation time steps.

The sample is composed of 71% feldspar (Fsp), 21% quartz (Qz) and 8% biotite (Bt), and the size of mineral grains obeys a normal distribution (see Fig. 20b). The model consists of 538 mineral grains with an average grain size of 1.2 mm, and each grain is further meshed into around 20 to 70 triangle elements in order to effectively capture the deformation and breakage of mineral grains. The model contains $29,838$ triangle elements, and the unstructured Delaunay triangulation mesh scheme is employed. To realistically capture the thermo-mechanical coupling procedure, we need to heat the granite sample to the target temperature using a convective

Table 7
Input parameters of granular particles for contact heat transfer simulation.

Input parameters	Value
Young's modulus, E (GPa)	30
Bulk density, ρ (kg/m^3)	2700
Poisson's ratio, ν	0.27
Viscous damping coefficient, η ($\text{kg}/\text{m}\cdot\text{s}$)	6400
Normal contact penalty, P_n (GPa)	300
Tangential contact penalty, P_s (GPa)	300
Thermal conductivity coefficient, k ($\text{W}/(\text{m}\cdot^\circ\text{C})$)	20
Heat capacity, C_p ($\text{J}/(\text{kg}\cdot^\circ\text{C})$)	880
Thermal expansion coefficient α , ($1/^\circ\text{C}$)	9.5×10^{-5}
Contact conductance coefficient, h_c , ($\text{W}/(\text{m}^2 \cdot ^\circ\text{C})$)	2.0×10^4
Solid time step Δt_s , (s)	6.0×10^{-8}
Thermal time step Δt_h , (s)	6.0×10^{-5}

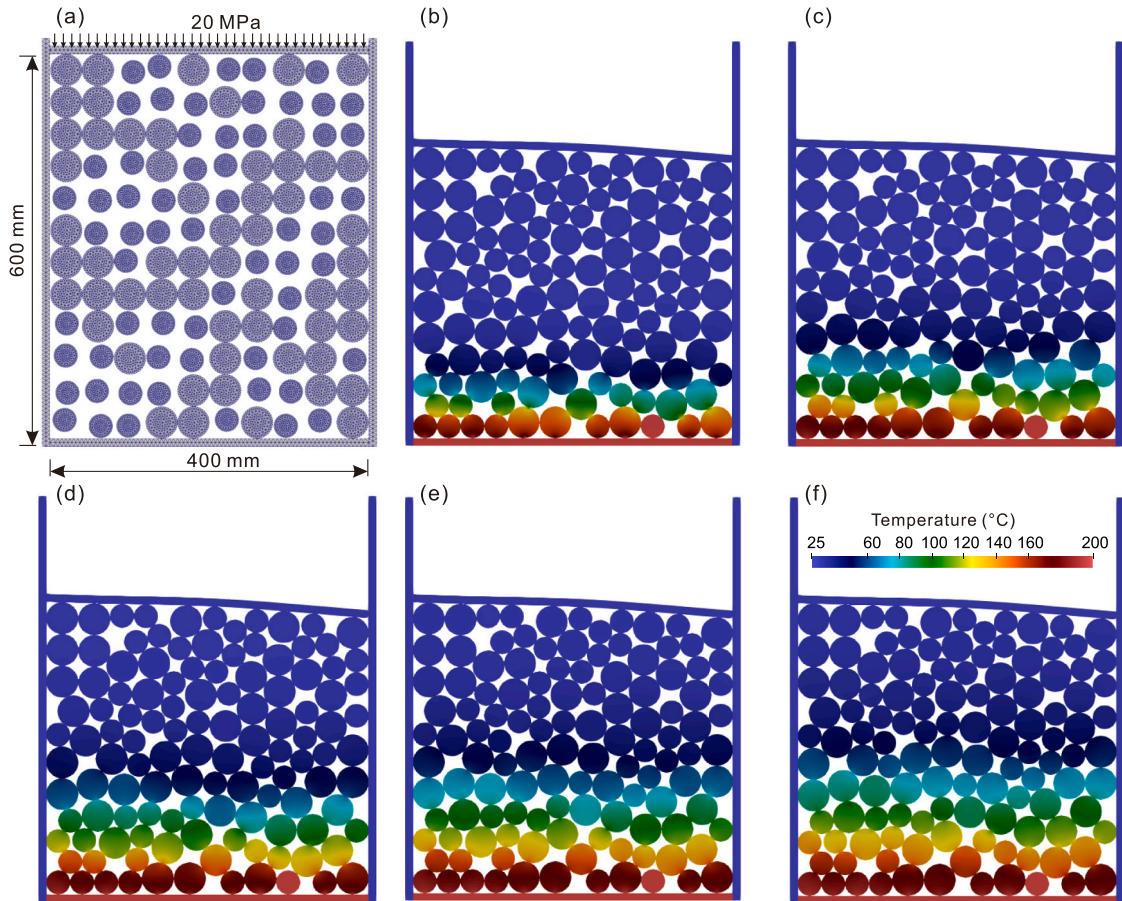


Fig. 17. (a) Model geometry and boundary conditions. Heat transfer process in the granular media at different timestamps: (b) 4800 s, (c) 9600 s, (d) 14400 s, (e) 19200 s and (f) 24000 s.

heat transfer boundary condition [43]. As shown in Fig. 20c, we adopt a heating rate of $3.75^\circ\text{C}/\text{s}$ to heat the sample from 25°C (room temperature) to 400°C , 500°C , 600°C and 700°C , respectively. The thermo-mechanical properties of each mineral are summarized in Table 9, which have been well-calibrated in previous works [43–45]. We use a plane-strain assumption model, and the mechanical and thermal time steps in this case are 2.0×10^{-9} s and 6.0×10^{-4} s, respectively.

To better understand the mechanism of thermal cracking, we adopt the acoustic emission (AE) simulation technique to evaluate the thermo-mechanical coupling process. This technique can not only capture the magnitude of AE events, but also distinguish macroscopic fracture types when an AE event contains multiple microcracks (broken of a cohesive element) based on moment tensor decomposition. Note that, a microcrack denotes the breakage of a single cohesive element, while an AE event indicates a cluster of one

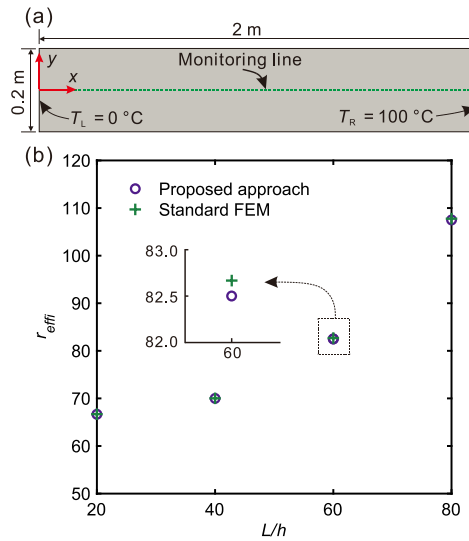


Fig. 18. (a) Model geometry (the monitoring line is marked in green dotted line). (b) Comparison of the computational efficiency between the proposed approach, the standard FEM and the original approach with various element sizes. L denotes the width of the rectangle plate; h is the element size; r_{eff} is the ratio of the computing time needed between the original and proposed approaches, as well as the standard FEM, upon heat conduction reaching a steady state. (For interpretation of the references to colour in this figure legend, the reader is referred to the web version of this article.)

Table 8
Time step size for various mesh sizes.

Mesh size (L/h)	Proposed approach/Sandared FEM (s)	Original approach (s)
20	1.0×10^{-1}	1.8×10^{-3}
40	2.0×10^{-2}	3.0×10^{-4}
60	9.8×10^{-3}	1.2×10^{-4}
80	5.0×10^{-3}	5.0×10^{-5}

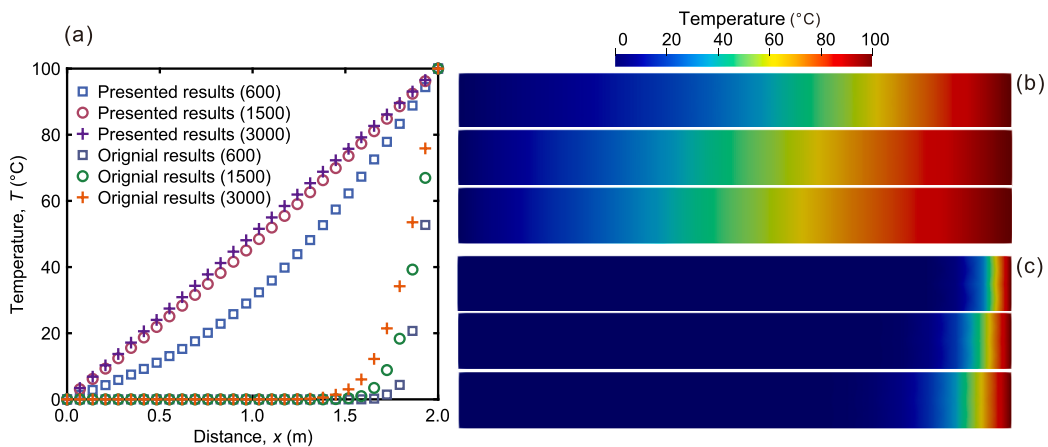


Fig. 19. (a) Comparison of temperature distribution between the proposed and original approaches at different steps with $L/h = 20, 600, 1500$ and 3000 . The temperature distribution is obtained from (b) the proposed approach and (c) the original approach at different steps.

or more cohesive element breakages, and the term “macroscopic fracture” represents the fracture generated associated with an AE event. More details about AE simulation are available in Appendix D and our previous work [46]. The failure patterns of transgranular (TG) and intergranular (IG) cracks for different target temperatures are presented in Fig. 21a. We can observe that IG cracks are dominant due to the low tensile strength at mineral boundaries, and the TG cracks mainly occur inside F_{sp} owing to its relatively lower tensile strength (5 MPa). With the increasing temperature ($>500\text{ }^\circ\text{C}$), more IG cracks are generated at weak boundaries. As shown in

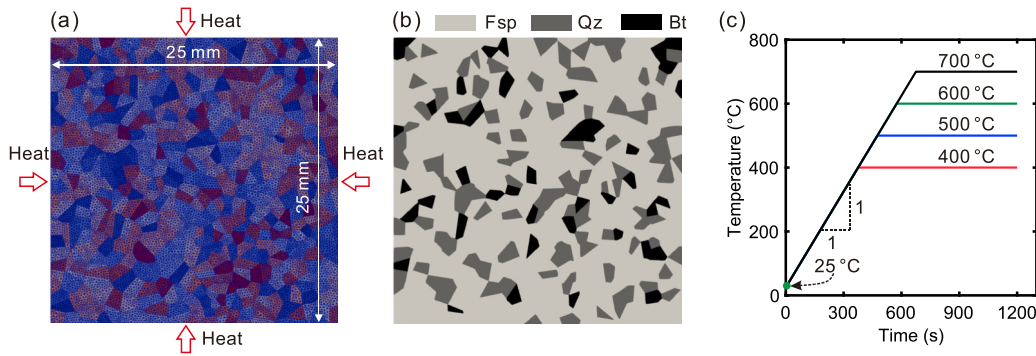


Fig. 20. (a) Model geometry and mesh. (b) Mineral grain distribution. (c) Heating schemes for thermal cracking; the room temperature at 25 °C is marked by a green dot. (For interpretation of the references to colour in this figure legend, the reader is referred to the web version of this article.)

Table 9
Mineral properties for heating simulation [modified from 43,44,45].

Input parameters (Unit)	Fsp	Qz	Bt			
Composition	71 %	21 %	8 %			
Young's modulus, E (GPa)	56.4	83.1	17.2			
Bulk density, ρ (kg/m ³)	2600	2600	2800			
Poisson's ratio, ν	0.32	0.25	0.36			
Tensile strength, f_t (MPa)	5.5	11.4	4.2			
Cohesion, c (MPa)	24.2	24.2	24.2			
Internal friction angle, φ (°)	51.8	51.8	51.8			
Mode I fracture energy, G_{I1} (J/m ²)	10	30	20			
Mode II fracture energy, G_{I2} (J/m ²)	20	60	40			
Normal contact penalty, P_n (GPa)	56.4	83.1	17.2			
Tangential contact penalty, P_s (GPa)	564	831	172			
Thermal conductivity coefficient, k (W/(m·°C))	1.781	2.292	9.037			
Heat capacity, C_p (J/(kg·°C))	760.4	815.0	740.6			
Thermal expansion coefficient α , ($1/°C$)	1.3×10^{-5}	3.0×10^{-6}	2.0×10^{-5}			
	Interphase		Homophase			
	Fsp-Qz	Fsp-Bt	Qz-Bt	Fsp-Fsp	Qz-Qz	Bt-Bt
Tensile strength, f_t (MPa)	0.23	0.21	0.21	4.95	10.26	3.78
Cohesion, c (MPa)	19.3	19.3	19.3	19.3	19.3	19.3
Internal friction angle, φ (°)	40	40	40	48.7	48.7	48.7
Mode I fracture energy, G_{I1} (J/m ²)	6	5	5	8	20	10
Mode II fracture energy, G_{I2} (J/m ²)	12	10	10	16	40	20
Normal contact penalty, P_n (GPa)	56.4	17.2	17.2	28.2	41.6	8.6
Tangential contact penalty, P_s (GPa)	564	172	172	282	416	86

Fig. 21b, the AE event number gradually increases with increasing temperature, while the ratio of IG/TG crack number witnesses a decreasing trend. We deduce that the increasing temperature induces more microcracks and significantly promotes the initiation of TG cracks.

The macro-fracture types associated with AE events are presented in Fig. 21c. It can be seen that the number of all fracture types increases with the increasing temperature, and the numbers of tensile and tensile-shear fractures dominate under all heating conditions, which is due to the low tensile to shear strength of the minerals. To further analyze the evolution of cracks and temperature, we take $T = 600\text{ °C}$ for example to capture the crack propagation and temperature under different timestamps shown in Fig. 22. It can be observed that microcracks are randomly initiated from the sample due to different thermal expansion coefficients of minerals when temperature is heated around 210 °C to 260 °C (Fig. 22a). As temperature continues to increase (Fig. 22c-d), more microcracks initiate and yield more isolated mineral grains.

5. Conclusions

In this study, within the framework of FDEM, a new thermo-mechanical coupling model is proposed and implemented to simulate heat conduction, thermal cracking and contact heat transfer. In this proposed model, a node binding scheme is adopted to ensure the continuum behavior of heat conduction in the intact/continuous rock matrix domain prior to fracturing, and thus can effectively enhance computational efficiency without introducing the extra heat exchange coefficient for cohesive elements.

A series of numerical benchmark examples are conducted to verify the correctness and accuracy of the proposed thermo-mechanical coupling model. The temperature distributions in a thick-wall disc and rectangular sheet based on the FDEM

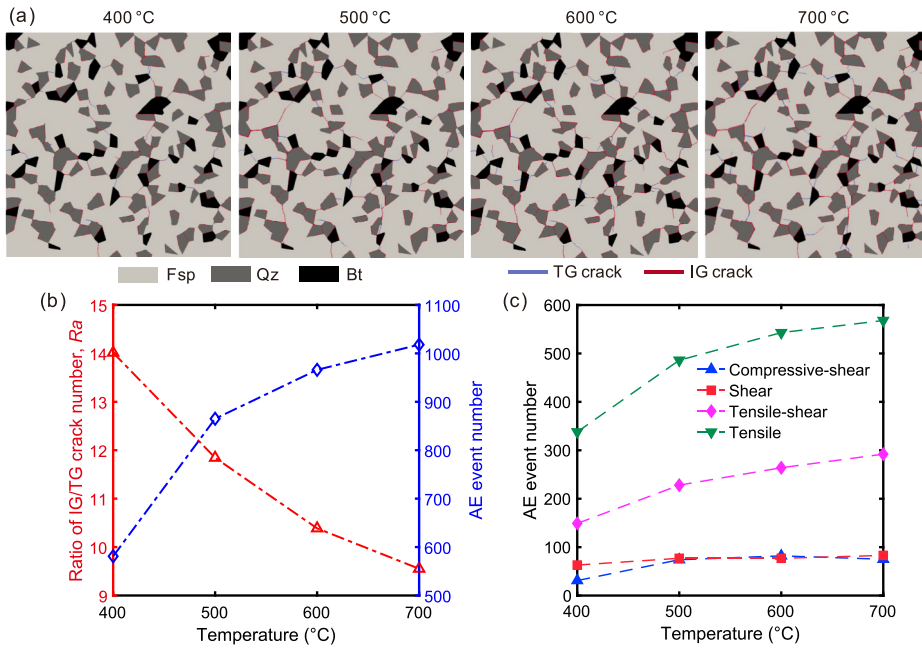


Fig. 21. (a) The transgranular (TG) and intergranular (IG) cracks induced by different temperatures from 400 °C to 700 °C. (b) AE number and the ratio of IG/TG crack number at different temperatures. (c) The number of micro-fracture types varies with temperatures.

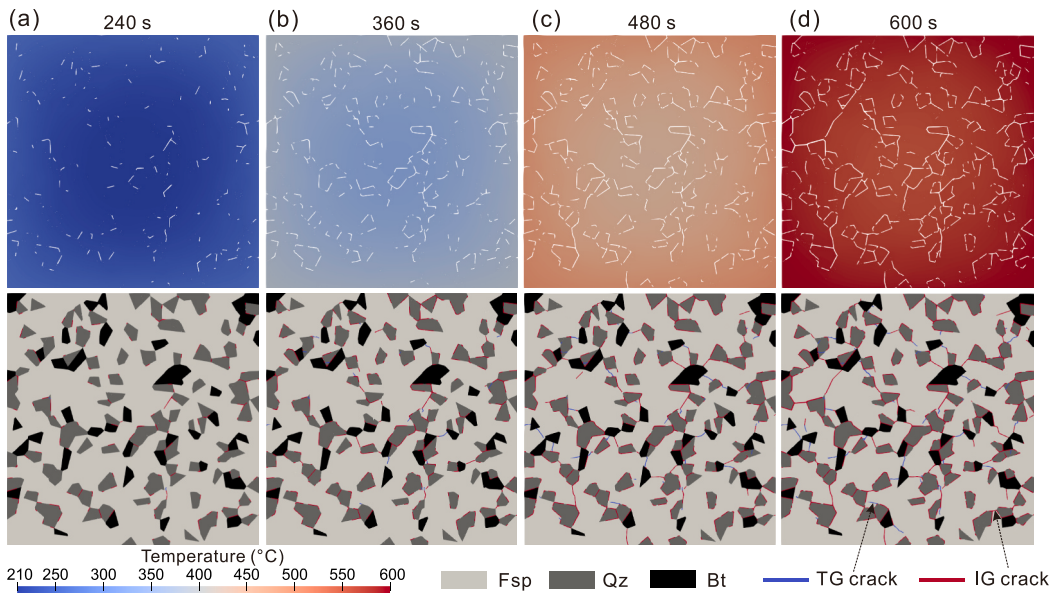


Fig. 22. Evolution of temperature and cracks at different timestamps ($T = 600$ °C): (a) 240 s, (b) 360 s, (c) 480 s and (d) 600 s.

simulations agree with the analytical solutions, which verify the accuracy of heat conduction in continuous media. To consider rock fracturing, the disc specimens suffered from thermal shock are performed to test the capability of the proposed approach for simulating crack imitation and propagation induced by a temperature gradient, and the fracture paths and failure patterns are also consistent with previous numerical and experimental observations. The heat transfer between granular particles is also simulated, in which the temperature of granular particles gradually increases from the bottom to the top of the barrel, demonstrating its capability of capturing heat transfer between discrete bodies.

Following this, one application example is conducted to demonstrate the mechanism of thermal cracking in crystalline rocks with micro-heterogeneity. The intergranular (IG) cracks dominate at various temperatures, and more isolated mineral grains are generated with the increasing temperature. The number of AE events also gradually increases with the increasing temperature, whereas the ratio

of IG/TG crack number witnesses a decreasing trend. The proposed thermo-mechanical coupling model may help enhance its applicability for estimating the propagation of thermal cracking associated with deep energy processing (e.g., hot dry rock and nuclear waste storage).

Author contributions

The authors confirm contributions to the paper as below: Research design: Ke Gao and Yu Feng; Analysis of numerical results: Weibing Cai and Shuai Zhang; Draft manuscript preparation: Weibing Cai and Shugang Ai; Revised manuscript and funding support: Ke Gao. All authors have reviewed the results and approved the final version of the manuscript.

CRedit authorship contribution statement

Weibing Cai: Writing – original draft, Software. **Ke Gao:** Writing – review & editing, Funding acquisition. **Shugang Ai:** Methodology, Formal analysis. **Shuai Zhang:** Validation. **Yu Feng:** Formal analysis.

Declaration of competing interest

The authors declare that they have no known competing financial interests or personal relationships that could have appeared to influence the work reported in this paper.

Acknowledgments

This work is supported by the National Science and Technology Major Project of China (2024ZD1000400), the Shenzhen Science and Technology Program (JCYJ20220530113612028), and the High Level of Special Funds (G03034K001) in SUSTech.

Appendix A.: Explicit solution

In FDEM, we employ the explicit integration schemes to solve the nodal motion equations, i.e.,

$$\mathbf{M}\ddot{\mathbf{u}} + \mathbf{C}\dot{\mathbf{u}} = \mathbf{f} \quad (\text{A.1})$$

where \mathbf{M} is the lumping mass matrix, \mathbf{C} is the damping matrix, \mathbf{u} is the nodal displacement vector, and \mathbf{f} represents the total nodal force vector (including the contribution from thermal expansion). The central difference scheme is utilized to update the nodal displacements and velocities at each simulation time step. That is, the velocity vector $\dot{\mathbf{u}}$ of each node can be obtained by

$$\dot{\mathbf{u}}(t + \Delta t) = \dot{\mathbf{u}}(t) + \ddot{\mathbf{u}}(t) \cdot \Delta t \quad (\text{A.2})$$

where Δt is the solid time step [31], and t and $t + \Delta t$ denote the previous and current time instants, respectively. Then, we can update the displacement vector $\mathbf{u}(t + \Delta t)$ using

$$\mathbf{u}(t + \Delta t) = \mathbf{u}(t) + \dot{\mathbf{u}}(t) \cdot \Delta t \quad (\text{A.3})$$

Appendix B.: Mesh sensitivity analysis for heat conduction simulation

To conduct the mesh sensitivity analysis for heat conduction, we establish a rectangular plate with dimensions of 1 m \times 0.25 m (length \times width), as shown in Fig. B1a. We impose two constant temperatures of T_L (0 °C) and T_R (100 °C) on the left and right boundaries of the plate, respectively, and record the temperature distribution under steady-state conditions along the monitoring line. The input parameters tabulated in Table 2 are used here. As shown in Fig. B1b, we first vary four mesh sizes, i.e., $L/h = 2, 4, 6$ and 8 , to analyze the effect of mesh size on the simulated accuracy of heat conduction (L is the width of the plate, and h is the average mesh size). As plotted in Fig. B1c & d, we can observe that the simulated temperatures with respect to temperature distribution along the monitoring line are in good agreement with the analytical solution using various mesh sizes, and the maximum relative errors (defined in Section 3) are merely $\sim 10^{-5}$ with the decrease of mesh size (i.e., increase of L/h). Such minor relative errors suggest that the heat conduction simulated by our proposed method exhibits good convergence in terms of mesh size. To further evaluate the effect of mesh shape on simulated accuracy, we utilize three mesh shapes (i.e., referred to as S-1, S-2 and S-3, respectively) to compare the simulated temperature with the analytical solution (see Fig. B1e). As shown in Fig. B1f, we find good consistency between the simulated temperature and the analytical solution under these three mesh shapes. The maximum relative errors remain unchanged at $\sim 1.22 \times 10^{-5}$ (see Fig. B1g), indicating that the element shape has little effect on the simulated results in terms of heat conduction using our proposed approach.

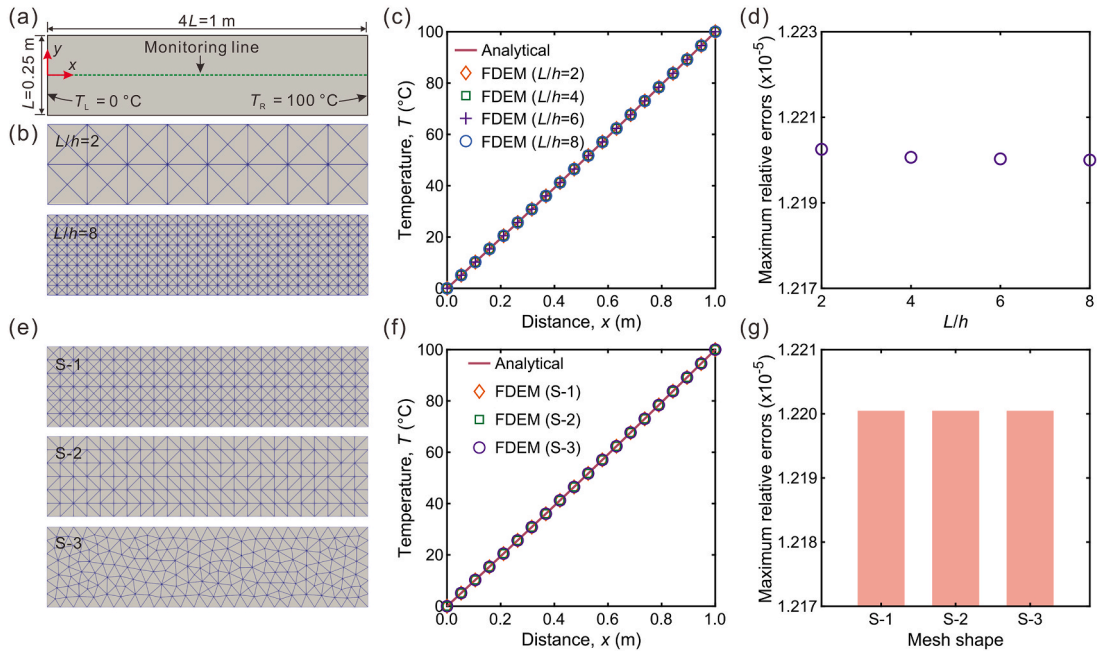


Fig. B1. (a) Model geometry and boundary conditions (the dotted line is the monitoring line). (b) Various mesh sizes: $L/h = 2$ and 8. (c) Comparison of temperature distribution between FDEM results and analytical solution under different mesh sizes. (d) Maximum relative errors vary with various mesh sizes. (e) Different mesh shapes: S-1, S-2 and S-3. (f) Comparison of temperature distribution between FDEM results and analytical solution under different mesh shapes. (g) Maximum relative errors vary with different mesh shapes. L is the width of the plate, and h is the average mesh size.

Appendix C.: Mesh sensitivity analysis for solid fracturing simulation

We perform a series of regular uniaxial compression tests to investigate the effect of mesh size on solid fracturing simulation. As shown in Fig. C1a, The width and height of the models are respectively 60 mm and 120 mm. We impose axial compression loads on the top and bottom of each specimen through two rigid platen moving in opposite directions at a constant velocity of 0.05 m/s. The selected loading velocity is reasonable, although larger than that in physical experiments [32,47]. We employ the unstructured Delaunay triangulation scheme to mesh these models (see Fig. C1b), and use five mesh sizes, i.e., $h = 1.8\text{ mm}$, 1.6 mm , 1.4 mm , 1.2 mm and 1.0 mm (h is the average mesh size). We assume that the simulated material is homogeneous and isotropic in this case. The parameters used for this model are tabulated in Table C1, which has been well-calibrated in previous literature [48]. As shown in Fig. C1c & d, the stress–strain curves exhibit a similar trend for the different models with various mesh sizes, and the peak strength is unchanged when the mesh size h is less than 1.4 mm , indicating that the mechanical response is not affected by the mesh size ($h \leq 1.4\text{ mm}$). That is, if L/h is larger than 42.8 (L is the width of the model), our proposed approach can generate reasonable results in crack propagation simulation. In particular, the simulated peak strength varies from 23.82 MPa to 24.45 MPa for models with these five mesh sizes, which is consistent with the analytical solution (i.e., 22.86 MPa calculated by the equation $2c \cdot \cos\varphi / (1 - \sin\varphi)$, where c is the cohesion and φ is the internal friction angle).

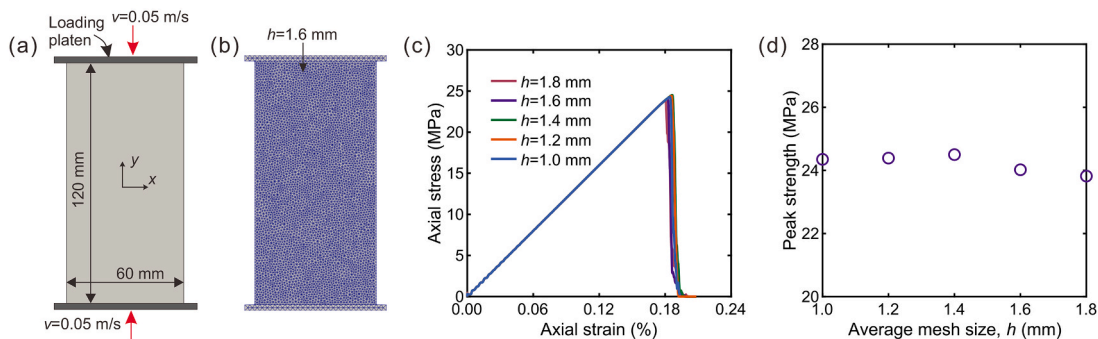


Fig. C1. (a) Model geometry and boundary conditions. (b) Mesh ($h = 1.6\text{ mm}$). (c) Stress strain curves under various mesh sizes ($h = 1.8\text{ mm}$, 1.6 mm , 1.4 mm , 1.2 mm and 1.0 mm) (d) Comparison of peak strength under various mesh sizes.

Table C1
Input parameters in uniaxial compression tests [48].

Input parameters	Values
Young's modulus, E (GPa)	12.5
Bulk density, ρ (kg/m ³)	2400
Poisson's ratio, ν	0.25
Viscous damping coefficient, η (kg/m.s)	5500
Tensile strength, f_t (MPa)	2
Cohesion, c (MPa)	7
Internal friction angle, ϕ (°)	27
Mode I fracture energy, G_{f1} (J/m ²)	30
Mode II fracture energy, G_{f2} (J/m ²)	90
Normal contact penalty, P_n (GPa)	18
Tangential contact penalty, P_s (GPa)	62.5

Appendix D:. Moment tensor based AE simulation approach

In FDEM, we employ the cohesive elements inserted at the common boundaries between adjacent finite elements to characterize crack initiation and propagation. Therefore, the generation of AE events involves the damage softening and energy release of cohesive elements. We note that one AE event may contain one or more microcracks (i.e., breakage of cohesive elements). Therefore, we combine multiple microcracks that occurred close in space and time as a distinct AE event. As shown in Fig. D1a, if the cohesive element evolves from the damage initiation point to the breakage point, the normal traction will decrease from tensile strength f_t to zero, thereby yielding a progressive change of local nodal force. Then, we can calculate the moment tensor of this AE event based on the changes and nodal forces when an AE event contains only a single microcrack (see Fig. D1b) [49], i.e.,

$$\mathbf{M}_{ij} = \Delta F_{ik} \mathbf{L}_{kj} \quad i, j = 1, 2 \tag{D.1}$$

where ΔF_{ik} represents the components of nodal force variance of each node; \mathbf{L}_{kj} is the components of distance measured from each node to the AE event center; the subscript k denotes the number of nodes contained in each AE event. If an AE event contains multiple microcracks (e.g., Fig. D1c), we only need to update the AE center by considering all the involved cohesive elements. Then, we can further distinguish the macro-fracture types by defining variable R , i.e.,

$$R = \frac{100 \times \text{tr}(\mathbf{M})}{|\text{tr}(\mathbf{M})| + \sum_{i=1}^2 |m_i^*|} \tag{D.2}$$

where R is the ratio of the isotropic to the deviatoric component of the moment tensor [50]; $\text{tr}(\mathbf{M})$ denotes the trace of the moment tensor, i.e., $\text{tr}(\mathbf{M}) = \sum m_i$ ($i = 1, 2$ for 2D cases) and m_i represents the eigenvalue of the moment tensor; $m_i^* = m_i - \text{tr}(\mathbf{M})/2$. As illustrated in Fig. D2, an AE event can be classified into four typical types, i.e., compressive-shear type if $-100 \leq R \leq -30$, shear type if $-30 < R \leq 20$, tensile-shear type if $20 < R \leq 30$, and tensile type if $30 < R \leq 100$.

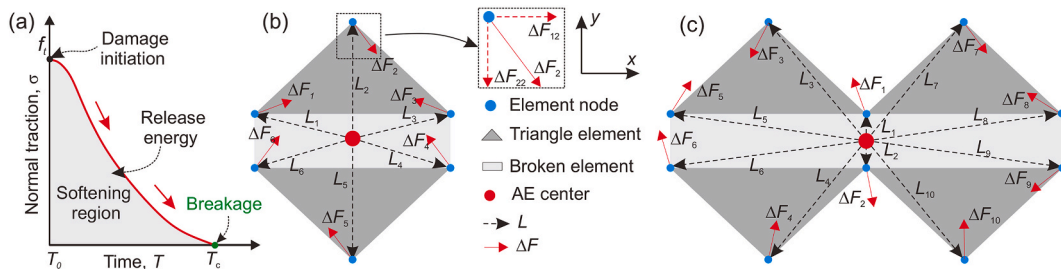


Fig. D1. (a) Normal traction of cohesive elements evolves via time when the tensile failure occurs. Schematic of moment tensor calculation for AE events containing (b) one microcrack or (c) multiple microcracks. f_t is the tensile strength of cohesive elements, ΔF and L are the vector of node force change and the distance from a node to the AE center, respectively. The vector of node force variance and the distance can be further decomposed into components along the x and y axis directions, which correspond to the components of ΔF_{ik} and \mathbf{L}_{kj} in Eq. (D.1).

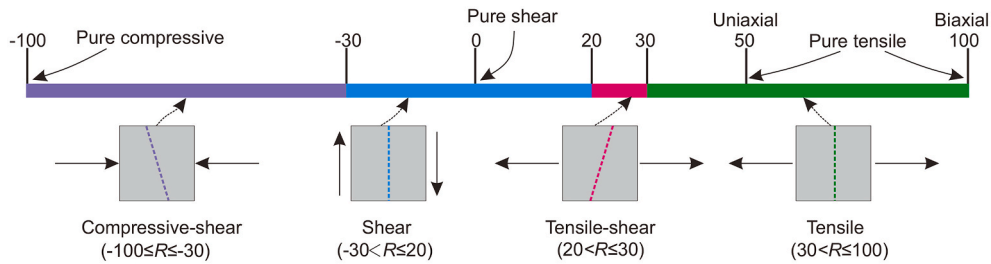


Fig. D2. AE type distinguishment according to R value.

Data availability

Data will be made available on request.

References

- [1] Nasseri MHB, Tatone BSA, Grasselli G, Young RP. Fracture toughness and fracture roughness interrelationship in thermally treated westerly granite. *Pure Appl. Geophys.* 2009;166(5):801–22.
- [2] Hudson JA, Cosgrove JW, Kemppainen K, Johansson E. Faults in crystalline rock and the estimation of their mechanical properties at the Olkiluoto site, western Finland. *Engng Geol* 2011;117(3):246–58.
- [3] Bou Jaoude I, Novakowski K, Kueper B. Identifying and assessing key parameters controlling heat transport in discrete rock fractures. *Geothermics* 2018;75: 93–104.
- [4] An Z, Yu T, Bui TQ, Wang C, Trinh NA. Implementation of isogeometric boundary element method for 2-D steady heat transfer analysis. *Adv Engng Softw* 2018; 116:36–49.
- [5] Ekneligoda TC, Marshall AM. A coupled thermal-mechanical numerical model of underground coal gasification (UCG) including spontaneous coal combustion and its effects. *Int. J. Coal Geol.* 2018;199:31–8.
- [6] Jiang W, Spencer BW, Dolbow JE. Ceramic nuclear fuel fracture modeling with the extended finite element method. *Engng Fract Mech* 2020;223:106713.
- [7] Li W, Shirvan K. Multiphysics phase-field modeling of quasi-static cracking in uranium ceramic nuclear fuel. *Ceram. Int.* 2021;47(1):793–810.
- [8] Wang Y, Zhou X, Kou M. An improved coupled thermo-mechanic bond-based peridynamic model for cracking behaviors in brittle solids subjected to thermal shocks. *Eur J Mech A-Solids* 2019;73:282–305.
- [9] Cundall PA, Strack ODL. A discrete numerical model for granular assemblies. *Geotechnique* 1979;29(1):47–65.
- [10] Yin T-B, Zhuang D-D, Li M-J, Li X-B. Numerical simulation study on the thermal stress evolution and thermal cracking law of granite under heat conduction. *Comput. Geotech.* 2022;148:104813.
- [11] Dang Y, Yang Z, Liu X. Revealing the influence of grain size on failure mechanisms and acoustic emission characteristics in thermally treated crystalline rock: insights from moment tensor inversion. *Rock Mech Rock Engng* 2024;57(5):3937–69.
- [12] Board M. UDEC (Universal Distinct Element Code) Version ICG1.5. Nuclear Regulatory Commission, Washington, DC (USA); 1989.
- [13] Shi GH, Goodman RE. Two dimensional discontinuous deformation analysis. *Int. J. Numer. Anal. Methods Geomech.* 1985;9(6):541–56.
- [14] Munjiza A. Discrete elements in transient dynamics of fractured media. Swansea, UK: Swansea University; 1992. PhD thesis.
- [15] Fukuda D, Liu H, Zhang Q, Zhao J, Kodama J-i, Fujii Y, et al. Modelling of dynamic rock fracture process using the finite-discrete element method with a novel and efficient contact activation scheme. *Int. J. Rock Mech. Min. Sci.* 2021;138:104645.
- [16] Yan C, Zheng H. A coupled thermo-mechanical model based on the combined finite-discrete element method for simulating thermal cracking of rock. *Int. J. Rock Mech. Min. Sci.* 2017;91:170–8.
- [17] Sun L, Liu Q, Grasselli G, Tang X. Simulation of thermal cracking in anisotropic shale formations using the combined finite-discrete element method. *Comput. Geotech.* 2020;117:103237.
- [18] Wang Z, Liu Q, Wang Y. Thermo-mechanical FDEM model for thermal cracking of rock and granular materials. *Powder Technol.* 2021;393:807–23.
- [19] Yan C, Zheng Y, Huang D, Wang G. A coupled contact heat transfer and thermal cracking model for discontinuous and granular media. *Comput Meth Appl Mech Eng* 2021;375:113587.
- [20] Yan C, Wang X, Huang D, Wang G. A new 3D continuous-discontinuous heat conduction model and coupled thermomechanical model for simulating the thermal cracking of brittle materials. *Int. J. Solids Struct.* 2021;229:111123.
- [21] Yan C, Yang Y, Wang G. A new 2D continuous-discontinuous heat conduction model for modeling heat transfer and thermal cracking in quasi-brittle materials. *Comput. Geotech.* 2021;137:104231.
- [22] Cai W, Gao K, Ai S, Wang M, Feng YT. Implementation of extrinsic cohesive zone model (ECZM) in 2D finite-discrete element method (FDEM) using node binding scheme. *Comput. Geotech.* 2023;159:105470.
- [23] Yan C, Jiao Y-Y. A 2D discrete heat transfer model considering the thermal resistance effect of fractures for simulating the thermal cracking of brittle materials. *Acta Geotech.* 2019;15(5):1303–19.
- [24] Wu Z, Cui W, Weng L, Liu Q. A 2D FDEM-based THM coupling scheme for modeling deformation and fracturing of the rock mass under THM effects. *Comput. Geotech.* 2022;152:105019.
- [25] Joulin C, Xiang J, Latham J-P. A novel thermo-mechanical coupling approach for thermal fracturing of rocks in the three-dimensional FDEM. *Comput Part Mech* 2020;7(5):935–46.
- [26] Liu Z, Ngai YWL. A new thermomechanical coupled FDEM model for geomaterials considering continuum-discontinuum transitions. *J Rock Mech Geotech Engng* 2024;16(11):4654–68.
- [27] Yan C, Xie X, Ren Y, Ke W, Wang G. A FDEM-based 2D coupled thermal-hydro-mechanical model for multiphysical simulation of rock fracturing. *Int. J. Rock Mech. Min. Sci.* 2022;149:104964.
- [28] Munjiza A. The combined finite-discrete element method. London: Wiley; 2004.
- [29] Munjiza A, Knight EE, Rougier E. Computational Mechanics of Discontinua. London: Wiley; 2011.
- [30] Fukuda D, Mohammadnejad M, Liu H, Zhang Q, Zhao J, Dehkhoda S, et al. Development of a 3D hybrid finite-discrete element simulator based on GPGPU-parallelized computation for modelling rock fracturing under quasi-static and dynamic loading conditions. *Rock Mech Rock Engng* 2019;53(3):1079–112.
- [31] Cai W, Gao K, Ai S, Zhi S. A 2D energy-conserving contact model for the combined finite-discrete element method (FDEM). *Comput. Geotech.* 2024;166:105972.

- [32] Tatone BSA, Grasselli G. A calibration procedure for two-dimensional laboratory-scale hybrid finite–discrete element simulations. *Int. J. Rock Mech. Min. Sci.* 2015;75:56–72.
- [33] Tao S, Tang X, Rutqvist J, Hu M, Liu Q. Simulating three dimensional thermal cracking with TOUGH-FEMM. *Comput. Geotech.* 2020;124:103654.
- [34] Li L, Tang C, Tang S, Lindqvist PA. Damage coupled thermo-mechanical model for rock failure process and applications. *Chin J Theor Appl Mech* 2006;38(4): 505–13.
- [35] Crank J. *The mathematics of diffusion*. Oxford, UK: Oxford University Press; 1975.
- [36] Boley BA, Weiner JH, Prager W. Theory of thermal stresses. *J. Appl. Mech.* 1961;28(2):318.
- [37] Abdalla H. Concrete cover requirements for FRP reinforced members in hot climates. *Comput. Struct.* 2006;73(1):61–9.
- [38] Liu Y, Wu X, Guo Q, Jiang C, Song F, Li J. Experiments and numerical simulations of thermal shock crack patterns in thin circular ceramic specimens. *Ceram. Int.* 2015;41(1):1107–14.
- [39] Carlson SR, Jansen DP, Young RP. *Thermally induced fracturing of lac du bonnet granite*. Kingston, Canada: Queen's University; 1993.
- [40] Wang Y, Zhou X, Kou M. A coupled thermo-mechanical bond-based peridynamics for simulating thermal cracking in rocks. *Int. J. Fract.* 2018;211(1–2):13–42.
- [41] Xia M, Zhao C, Hobbs BE. Particle simulation of thermally-induced rock damage with consideration of temperature-dependent elastic modulus and strength. *Comput. Geotech.* 2014;55:461–73.
- [42] Quey R, Dawson PR, Barbe F. Large-scale 3D random polycrystals for the finite element method: Generation, meshing and remeshing. *Comput Meth Appl Mech Eng* 2011;200(17–20):1729–45.
- [43] Aboyanah KR, Popoola AK, Abdelaziz A, Sun L, Ossetchkina E, Peterson K, et al. Effect of pre-existing cracks on thermal cracking of granitic rocks under confinement. *Geomech. Geophys. Geo-Energy Geo-Resour.* 2022;8(4):126.
- [44] Abdelaziz A, Zhao Q, Grasselli G. Grain based modelling of rocks using the combined finite-discrete element method. *Comput. Geotech.* 2018;103:73–81.
- [45] Lisjak A, Liu Q, Zhao Q, Mahabadi OK, Grasselli G. Numerical simulation of acoustic emission in brittle rocks by two-dimensional finite-discrete element analysis. *Geophys. J. Int.* 2013;195(1):423–43.
- [46] Cai W, Gao K, Wu S, Long W. Moment tensor-based approach for acoustic emission simulation in brittle rocks using combined finite-Discrete Element Method (FDEM). *Rock Mech Rock Engng* 2023;56:3903–25.
- [47] Mahabadi OK, Lisjak A, Munjiza A, Grasselli G. Y-Geo: new combined finite-discrete element numerical code for geomechanical applications. *Int. J. Geomech.* 2012;12(6):676–88.
- [48] Liu Q, Deng P. A numerical investigation of element size and loading/unloading rate for intact rock in laboratory-scale and field-scale based on the combined finite-discrete element method. *Engng Fract Mech* 2019;211:442–62.
- [49] Hazzard JF, Young RP. Moment tensors and micromechanical models. *Tectonophysics* 2002;356:181–97.
- [50] Feignier B, Young RP. Moment tensor inversion of induced microseismic events: evidence of non-shear failures in the $-4 < M < -2$ moment magnitude range. *Geophys. Res. Lett.* 1992;19(14):1503–6.